6-17-2021

Design of a pneumatic soft robotic actuator using model-based optimization

Mahsa Raeisinezhad
Rowan University

DESIGN OF A PNEUMATIC SOFT ROBOTIC ACTUATOR USING MODEL-BASED OPTIMIZATION

by

Mahsa Raeisinezhad

A Thesis

Submitted to the
Department of Mechanical Engineering
Henry M. Rowan College of Engineering
In partial fulfillment of the requirement
For the degree of
Master of Science in Mechanical Engineering
at
Rowan University
June 2nd, 2021

Thesis Chair: Mitja Trkov, Ph.D.

Committee Members:
Francis (Mac) Haas, Ph.D.
Behrad Koohbor, Ph.D.
Chen Shen, Ph.D.

Dedications

I would like to dedicate this manuscript to my family, whose unconditional love and support has made this possible. I would like to thank my parents, Sedigheh Amiri and Hassan Raeisinezhad, for always pushing me to be better, even beyond what I thought was possible. I would also like to thank my younger brother, Benyamin Raeisinezhad, for supporting me when I needed it most and always acting more mature than me. Thank you all, as I wouldn't be at this point if not for everything you have done for me.

Acknowledgements

I would like to express my gratitude to my advisor and mentor, Dr. Mitja Trkov. Your constant guidance and support over the past two years has made me a better researcher and engineer. Working in your lab has been a wonderful experience, the knowledge I have gained and the work I have accomplished with your guidance is proving to be invaluable. I would also like to thank Dr. Behrad Koohbor, for his support and expertise into the research I have conducted. Further, I would like to thank Dr. Ratneshwar Jha for his support throughout my time at Rowan University.

I would like to extend a thank you to my friend and lab mates Troy Christiansen and Jordan Cook, for their expertise which aided in my research, and the memories we shared over the past two years and for the laughs and experiences we shared. Lastly, I would like to extend a special thank you to Nicholas Pagliocca, for being an amazing friend and coworker. His constant aid and support over the past two years has helped me through much of this research. He had a significant impact, either on this research or on me personally that I cannot put into words.

Abstract

Mahsa Raeisinezhad
DESIGN OF A PNUEMATIC SOFT ROBOTIC ACTUATOR USING MODEL-BASED OPTIMIZATION
2020-2021
Mitja Trkov, Ph.D.
Master of Science in Mechanical Engineering

In this thesis, the design and optimization process of a novel soft intelligent modular pad (IntelliPad) for the purpose of pressure injury prevention is presented. The structure of the IntelliPad consists of multiple individual multi-chamber soft pneumatic-driven actuators that use pressurized air and vacuum. Each actuator is able to provide both vertical and horizontal motions that can be controlled independently. An analytical modeling approach using multiple cantilever beams and virtual springs connected in a closed formed structure was developed to analyze the mechanical performance of the actuator. The analytical approach was validated by a finite element analysis. For optimizing the actuator's mechanical performance, firefly algorithm and deep reinforcement learning-based design optimization frameworks were developed with the purpose of maximizing the horizontal motion of the top surface of the actuators, while minimizing its corresponding effect on the vertical motion. Four optimized designs were fabricated. The actuators were tested and validated experimentally to demonstrate their required mechanical performance in order to regulate normal and shear stresses at the skin-pad interface for pressure injury prevention applications.

Table of Contents

Table of Contents (Continued)

Table of Contents (Continued)

Table of Contents (Continued)

List of Figures

List of Figures (Continued)

Figure Page

List of Tables

Table Page

Chapter 1

Introduction

1.1. Introduction to Soft Robotics

Rigid-link systems have dominated the bulk of the robotics of the 20th century. Over the last two decades, robotics has experienced a fundamental shift in the aspect of the actuation principles and materials used for their fabrication [1]. These new intelligent systems (i.e., soft robots) are fundamentally different compared to their rigid-body counterparts, due to employing ideas and principles from biology [2]. Utilizing materials with significantly reduced stiffness enabled the creation of soft structures that have the capabilities to mimic soft biologic structures [3]. Soft materials enable highly versatile and compliant mechanisms that rigid-link systems have principally failed to capture. Such applications include grasping delicate objects and compliant human-machine interactions [4, 5]. Due to the high load resiliency, decrease in size and other unique features, the soft actuators enabled the development of the artificial muscles and micro robots as some examples [6]. By addressing the limitations imposed by the use of stiff materials, soft robots are cementing their way into the future of various industries that depend on robotics [4, 7] and are opening new ways and opportunities to perform tasks that were previously not possible to be performed by the robots [8].

The exploitation of soft structures by animals to move more successfully in their complicated natural surroundings has inspired robotic scientists and researchers to integrate soft technologies into the design of soft robots. This allows malleable, adaptive interplay between the robots and complex environments. Embracing soft robotic

technologies will result in less complicated mechanical and algorithmic robotic design [9].

To date, a concise definition of what truly constitutes a soft system has not been fully established. For many researchers, softness not only presents the fundamental flexibility made by the structural representation of hard materials but also refers to the inherent flexibility of materials [10]. Others perceive this from a macroscopic perspective and define this as a focus on materials with acceptably low elastic moduli [11]. Presentation of the discrepancies in the intrinsic meaning of what constitutes "soft" aims to convey that such technologies are still in their relative infancy. In addition, it is worth noting here that there is also considerable interest amongst the robotics community to explore so-called soft-rigid systems. Such systems still fall under the general soft robotics domain and warrant their discussion. The rapid progress in the field of soft robotics presents considerable achievements in terms of the design, modeling, and fabrication of soft robots. This rapid progress can be attributed to pioneering works in the years 2009 to 2012 in the related fields from sensing, modeling, actuation, and control, as summarized in [12-15].

The matched characterization of soft robots and their intrinsic softness and compliance to their environment has enabled robots to squeeze, stretch, climb and grow; which historically was not possible using entirely rigid link systems [16]. The exploitation of these advantages has been fruitful in a plethora of applications [15]. One such example concerns the delicate manipulation and sampling of fragile species in marine applications [17]; see Figure 1. The motivation for such applications concerns the oil industry, where robots are employed for the sampling of deep reef species. Examples

of such advantages include enhancing the agility of healthy soldiers, ameliorating gait deficiencies, and addressing extreme debility to perform daily activities such as spinal cord injury patients [18]; see Figure 1.

Figure 1

Introductory Examples Showcasing Applications of Soft Robots

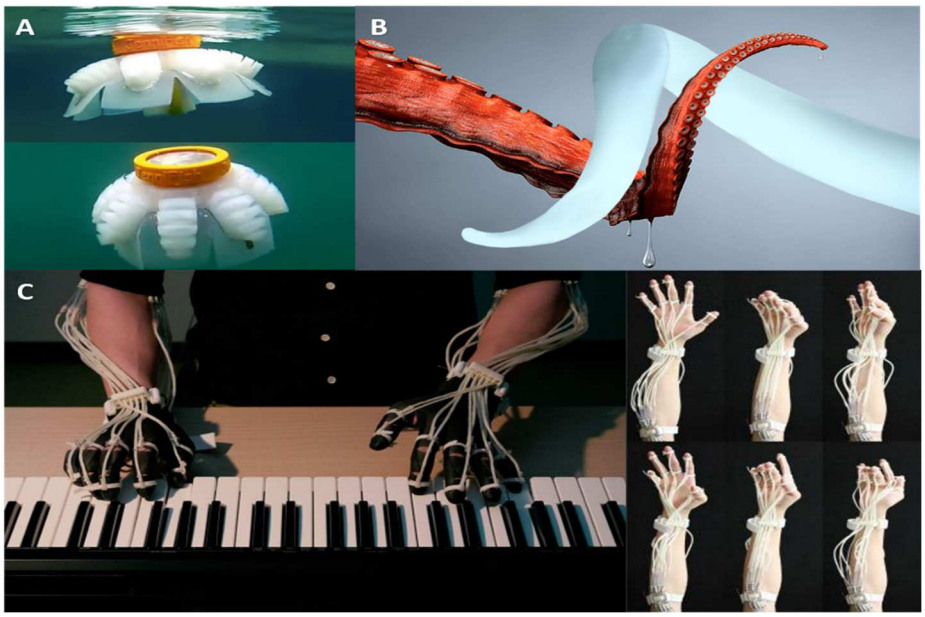

Note. Applications of soft systems with the capacity to replace rigid-link systems for A, Free swimming soft robotic jellyfish [19]. B, Octopus bioinspired soft robot arm [9]. C, Soft-exoskeletal devices as presented in [20].

The development of novel materials, structures, and advanced manufacturing techniques has continued to increase the application space of soft robotic technologies. These subsets of soft robotics research offer promising contributions such as embodied intelligence and tunable stiffness [21].

Soft robots can provide large deformations, various multifunctioning tasks, high movement complexity, and innovative applications in addition to their distinctive properties of multifunctionality [6]. Reasonable pricing for fabrication and simplicity of control for reaching a sophisticated application are some of the reasons that make soft robotics an interesting area of research for the soft robotic community [22]. Generally, soft robotic actuators can be categorized by the motion they can perform. These categories include bending, contraction, and elongation [23, 24], see Figure 2. This is expanded upon in the following sections.

Figure 2

Examples of Soft Robotic Actuators

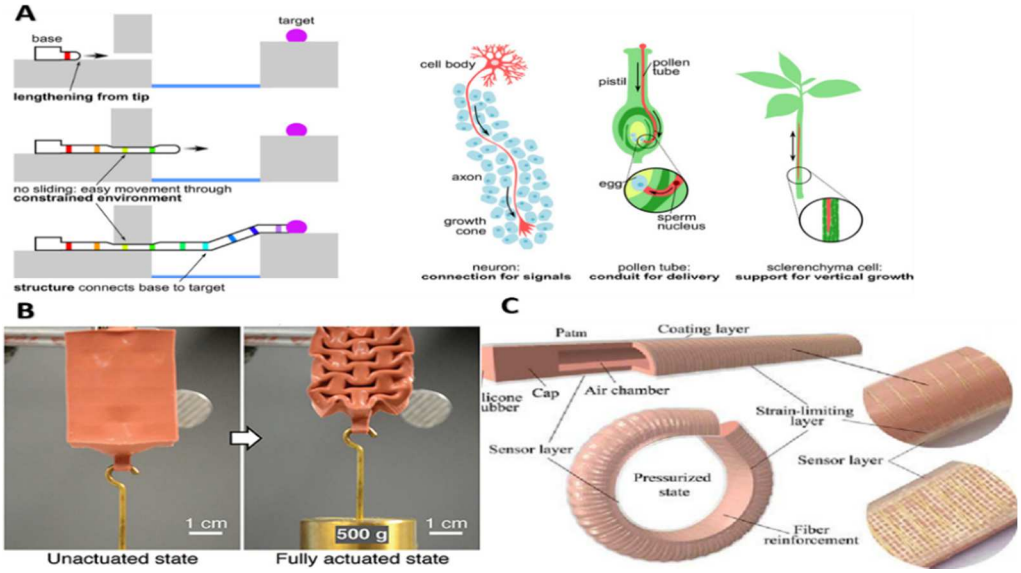

Note. These actuators are designed for the (a) elongation [17] (b) contraction [18], and (c) bending [19] tasks.

1.2. Design of Different Classes of Soft Actuators

The path of a soft actuators' motion relies on the topology of the actuator [4]. Within the three design paradigms presented - bending, contracting, and elongating devices - the design of elongating and contracting devices offers the simplest design principle [23]. The basis for this is that elongation and contraction-based devices traverse through the axis to which the pressure is applied. It should be noted that the design and modeling of contracting devices generally refer to Pneumatic Artificial Muscles (PAMs) [23, 25, 26]. Although various studies have provided methods for designing bending devices, a consensus has not been reached on a standard or generalizable design process [23]. Complex motions are also attainable through combinations of these paradigms; an example is a pressure-driven actuator that can achieve helical motions [27]. Furthermore, there exist novel designs of soft surface manipulators that provide saddle-like motions, wrapping, and rolling, which use shape morphing actuators to generate these motions [28]. To further expand the capabilities of soft robots and enhance their performance, novel motion modalities need to be developed.

In this thesis, a novel multi-degree-of-freedom (MDOF) actuator is presented, which can provide near-independent horizontal and vertical displacement based exclusively on air chamber topology. The actuator was designed as a modular element to be integrated into a larger array forming a complete system for surface manipulation. The actuator was first designed empirically [29] and then re-designed using a rigorous optimization process to reach its full potential [29, 30].

1.2.1. *Design of Contracting Devices*

Contracting Devices - generally PAMs'- are mostly made of soft inflatable chambers that provide linear motion by making the chamber longitudinally contract and radially expand when pressurized. This inflatable chamber converts pneumatic/hydraulic power from the pressurized fluid into generating mechanical work by contracting and pulling/exerting force on both ends [26]. A simple way to design PAMs is to use a theoretical-based approach following the conservation of energy. This approach provides relationships between tension, length, and the pressure applied on the inner surface of the chambers' walls [25]. Considering the force equilibrium on the fluid membrane of the actuator [23] can also be used to derive a structural framework for the design and modeling of contracting devices.

1.2.2. *Design of Bending Devices*

The most common application for bending devices is grasping. In the last decade, several different designs of fluid-driven soft robotic devices that can exhibit bending have been presented [31]. Flexible micro actuators (FMA) serve as one of the pioneering bending devices, and have been extensively studies [32]. FMA's are Electro-Pneumatic driven systems with three degrees of freedom. Specific characteristics of FMAs make them a suitable choice for such mechanisms as arms, fingers, and legs [33]. In [34], bending motion was achieved using three parallel PAMs in each section of the OctArm robot using a displacement-based design objective. PneuNets are another example of a well-researched bending device that consists of small chambers with interconnected channels to make a pneumatic network [35]. Using an elastomeric material to make these channels enables to provision of the desired motion with large amplitudes [36]. Proposed

Bending Fluid Actuators (BFA) are another category of miniature bending devices that use a parallel micro-channel design to achieve the desired bending motion. This specific design enables working at low pressure while having the highest torque per volume and angular displacement per length ratio. BFAs' can be adapted for minimally invasive surgery, if scaled down to smaller dimensions [37].

The lack of generalized and concurrent design methodologies in this emerging field has led that many soft actuators and systems were designed primarily based on engineering intuition or were bioinspired [9]. The development of rigorous design optimization methodology is required to systematically guide the design of soft robots to achieve optimal performance. Design methodology using finite element method has been developed for soft pneumatic actuators [38], however, they it is computationally demanding. In [22], quasi-static analytical models and non-linear finite-element methods were employed to propose a set of structured methodologies for designing and modeling bending devices for grasping applications. Nevertheless, the methodology proposed by [22] is not accepted as generalizable; as it mainly focuses on a set of predetermined designs [23]. Another design structure for fluid-driven bending devices has been provided in [23], which considers force equilibrium in the fluid membrane. The proposed approaches in the above-mentioned literature partially address design methodologies which are expanded upon in the following section.

1.2.3. *Concept Design of Elongating Devices*

Elongating devices comprise the simplest soft actuators since the displacement is directly based on the pressure applied to the specified chamber; whose direction is directly through the axis considered [23]. This actuation principle is mostly pneumatic or

hydraulic. Elongating devices are known to be amongst the actuators that provide the highest amount of force and power. Therefore, elongation devices could play an increasingly remarkable role in medical microsystems and modern industrial systems [39].

1.3. Computational and Analytical Modeling Introduction

1.3.1. *Empirical Methods*

Guidelines representing the use of empirical methods to design Elastic Inflatable Actuators (EIA) are detailed in the review [4]. These guidelines allow for the rapid development of soft actuators based on well-studied results. For example, it is suggested that to produce the optimal force from an expanded void, the length to width ratio of the chamber must be equal to almost 10 [40]. It has also been reported that to maximize the bending stroke, not only the bending rigidity between layers must vary with a factor of 2 to 3 [41], but also it increases when divided balloons are used [42]. The design methodology of actuators with variable stiffness concentration of material studied in [43] considered the fact that at lower pressures deformation occurs through the side with the lower stiffness and as the pressure increases to the higher amounts the deformation occurs towards the side possessing higher stiffness. If multi-material asymmetry would be considered in the design process this can be avoided from happening [44]. The overall importance of these considerations is that experimental studies that have characterized such actuators are useful for rapid development and design for a known topology. As design of soft robot is an emerging field, development of robust analytical methods to guide the design process can be an attractive alternative as it allows generalization.

1.3.2. *Analytical Methods*

Several modeling approaches have been considered in the literature to describe the static deformation and bending moments of actuators in soft robotic actuators. Euler-Bernoulli beam theory is arguably the most common [4]. Unfortunately, for large deflections the cross-sectional area does not stay perpendicular to the actuator's axis of rotation; therefore, Euler-Bernoulli beam theory is valid for small deflections and is less accurate when large deformations occur. It has been accepted that this method is suitable for qualitative analysis of soft manipulators, unsymmetrical irregular shape beams, multi-chambered actuators, and multi-material asymmetry [4, 45]. However, using Euler-Bernoulli's beam theory has provided new insight into the modeling of micro, fluid-driven soft actuators [46]. An analytical model based on Euler-Bernoulli's beam theory was proposed that can handle a deformable cross-sectional area [47]. Other documented methods used in design and control include the Timoshenko beam [48] and the Cosserat beam theory [49]. These formulations consider twist and shear, and for the latter, a continuum mechanics approach requires the use of advanced analytical methods. For modeling soft actuators discussed in this thesis, we use the Euler-Bernoulli beam theory over other approaches due to simplified modeling approach that allows to obtain closed form analytical solutions, while still generate good result approximation due to limited deflections consider in our study.

1.3.3. *FE Methods*

To compensate for the limitations imposed by methods such as Euler-Bernoulli, nonlinear FEM solvers can be used for improved computational modeling of quasi-static soft systems. Utilizing hyperelastic material models, such as Ogden [50] or Mooney-

Rivlin [51], make this method an attractive alternative and validation method for the design and modeling of soft actuators. Embedding these models in the FEM computational model requires identifying model parameters for a given material. Biaxial or uniaxial material testing experiments are performed on material samples to obtain model parameters. Testing data is commonly imported into a commercial FEM solver, ANSYS [52], over the archived data for hyperelastic materials to identify the hyperelastic material model parameters [36, 53-55]. FE dynamic models has also been explored in the literature, and is mentioned here for completeness [54, 56], but is out of the scope of this thesis and we focused on the static analysis, not considering the dynamic effects, due to relatively slow actuation of soft actuators.

1.4. Optimization of Soft Robots

To realize the optimal performance of a soft actuator, it is imperative to define a suitable design objective for its topology and structural properties [23]. Shape optimization is, therefore, a key metric in soft robotic actuators' performance and it is a remarkable consideration when it comes to improving the mechanical performance of soft robots. Although there is an abundance of optimization methods for many mathematical criteria, such as linear, nonlinear, multimodal, etc., there exists a lack of a generalizable method for design optimization of soft robotic actuators. These tools often lead to soft, long, slim, and unstable structures [57]. Using a numerical solution for a three-dimensional geometry coupled with a root-finding algorithm can realize the maximum desirable displacement of a cantilever beam subjected to a static vertical load as highlighted in [57]. Another optimization method provided for soft robotic applications is to derive the dynamic model of Cosserat beam based on the nonlinear

parameters of the beam geometry and then using its strain fields coupled with a topology optimization software [58]. To optimize the interaction of soft robots with the environment, [59] provided a novel chain-like structure for regulating the soft-rigid manipulator stiffness in a large range. In that theoretical modeling study, the best granules combination was found for use of chain-like structures using Euler-Bernoulli beam theory demonstrating the results experimentally. Another common analytical modeling optimizing soft actuators is using Lagrangian methods. [60] optimizes inflated balloons that undergo casting through an inverse problem using the Lagrangian method. They are cast in a way that when these optimized balloons are expanded, they must approximate the target geometry as much as possible. The validation of the results is through comparing the fabricated balloons and the predicted simulation results [60]. The underlying theme of almost all of the modeling methods and approaches mentioned above is that they require advanced numerical analysis techniques for the design objective alone. These procedures might be too complicated to be adapted for the practical design of soft robotic systems of any kind. Hence, in this thesis, a simple structural modeling approach of interconnected beams is provided, which has not been considered previously in other soft robotic studies.

The alternative design strategy presented by [61] is to optimize the geometry of the pneumatic actuator using finite element analysis and numerical methods and use additive manufacturing to fabricate it. Using genetic algorithm [62, 63] enabled to optimization of a multi-objective, multi-DOF bending device. A comparative study between evolutionary methods and swarm intelligence showed evolutionary methods are less precise than swarm intelligence algorithms [64]. Based on [65] using swarm

intelligence we can expect propitious solutions for the optimization of cantilever structures. In addition, a comparison between swarm methods such as classical particle swarm optimization, cuckoo search, accelerated particle swarm optimization, and firefly, the firefly algorithm was shown to be one of the most efficacious methods in model-based structural optimizations. The firefly algorithm was chosen in this study to optimize the structural modeling of three interconnected beams used in a soft pneumatic actuator, along with a deep reinforcement learning-based approach discussed in Chapter 5.

1.4.1. *FE Based Topology Optimization*

Using FE solvers mixed with density-based topology optimization has shown promising results for reaching the optimum output displacement for a pneumatic driven soft actuator while constraining the volume of the material [66]. A novel combination of soft robotic and topology optimization of pressure-driven actuators has been provided in [67]. That study has also provided the solution to overcome the difficulties and complexities related to hyper-elastic materials using penalization combined with the Solid Isotropic Material Method (SIMP). The developed framework in that study allows for the exploration of novel soft robotic morphologies [67]. The topology optimization method in [68] states that by combining MATLAB coding and Abaqus/CAE, and applying it to mathematical modeling of the structural design of soft gripper we can reach the optimal desired design. Another example includes [40] that used SIMP, but defined design variables as densities of discretized elements. While work in this thesis does not directly employ the use of topology optimization, it was considered as a possible method for achieving the actuators optimal performance.

1.5. Soft Robotics in Biomedical Applications

The inherent softness and compliance of soft robotic actuators make them a perfect fit for biomedical applications and human-machine interactions. For example, a recent study showed that hand robotic devices can be a solution for disabled people who are struggling with hand deficit or arm impairment [69]. Another study presented a soft pneumatic actuator capable of helping infants with their feeding process by inserting a light pressure, and a torsional stimulant on their sucking muscles [70]. Overall, recent developments in soft robotic actuators are enabling engineers to utilize them in various biomedical applications, including utilizing soft actuators in minimally invasive surgery [71], neurorehabilitation [72], wearable soft robotics [73], dental implantology [74], and pressure injury prevention mattresses [29]. Pressure injury prevention is one of the significant health problems concerning disabled people in the development of decubitus ulcers. Almost 2.5 million people need pressure injury treatment in the US per year [75]. The approximate related cost regarding the treatment of pressure injuries in the US was between $9.1 and $11.6 billion annually in the year 2007 [76]. The treatment of pressure injuries is exploited in this work and [29], and the motivation is presented in the following section.

1.5.1. *Biomedical Applications of Soft Robotic Actuators*

Along with the development of soft robotics different research groups have provided reviews such as potential applications of soft robotics in fields including healthcare [77]. As one of the biomedical applications of soft robotic actuators, we can point out pressure injury prevention mattresses. There are various factors causing decubitus ulcers such as immobility, nutritional deficit, neurological deficits, and skin

factors are the main patient factors causing pressure ulcers [78]. Furthermore, pressure ulcers are mainly caused by increased interface pressures, shear stress, and friction. This leads to the associated tissue degeneration and restriction of blood flow [78].

The existing clinical practices for pressure injury prevention include monitoring of the skin integrity, temperature, moisture, pressure distribution systems, using specific textiles with low friction for the dressing of the wound, and repositioning the patients constantly by human resources [79].

Other existing pressure injury prevention systems include air mattresses with variable pressure, passive foam, or inflating cushions and pads [80]. Only a few active systems are being used as a solution for this problem which only considers the effect of normal pressure [81, 82]. Repetitive contact shear stress has a remarkable effect on blister formation [83]. Due to the complexity of decubitus ulcer prevention systems, to the best of the author's knowledge, only two active systems exist that partially address this issue. One uses controllable soft air bladders and the other utilizes a multi-pin system that each pin is attached to small air bladders [81, 82]. However, none of them considers the skin-pad interface shear stress relaxation.

In this study, the design and optimization of a novel MDOF soft actuator is presented, which is proposed for further use in a soft modular pad [29]. This system can be used to regulate pressure to prevent decubitus ulcer formation and blisters in wheelchair users and bed-bound patients. Modeling, design, and experimental characterization of the actuators along with a detailed examination of optimization methods are presented in this thesis [29, 30].

The remaining chapters of this thesis are organized as follows: Chapter 2 gives an overview of both the design and optimization process of pressure injury prevention mattress's actuator, the required analytical modeling used in the optimization process. Chapter 3 provides information on the fabrication process and material characterization. Chapter 4 covers the two optimization methods used in this study and a comparison of the two methods is provided in this section as well as experimental validation results. Chapter 5 provides the results of the experiments and simulations. Chapter 6 introduces the business plan specified for the pressure injury prevention mattress. Chapter 7 presents the conclusion and future work.

Chapter 2

Design and Modeling of Soft Actuators

In this chapter, the design and modeling of an individual soft actuator will be presented to develop an overall injury prevention system. The overall goal of the soft actuator was to have the capabilities to decouple the horizontal and vertical motion of the actuator's top surface that are important features for a pressure injury prevention system. The results of this study were presented by Raeisinezhad et al. in [29, 30].

2.1. Design Process

Physical systems existing for pressure injury prevention encompass using pads that can inflate and deflate using alternating air/fluid pressure or using passive foams. It has been demonstrated that the active surfaces have some benefits over passive systems in decubitus ulcer prevention [80]. Few active systems exist for this purpose and amongst these systems, fewer systems have considered shear stress regulation [81, 82].

Considering this, the goal of this study was to design a soft intelligent robotic pad that regulates normal and shear stresses actively using air pressure and sensors [29]. IntelliPad, which stands for an intelligent modular soft robotic pad was designed as a structure including several independent actuators in a grid, see Figure 3. Each actuator is designed in a way that can achieve both independent horizontal and vertical motions. There is a pressure/force sensor integrated on top of each actuator for control purposes. The information gained from each sensor is used to control displacements of each actuator top portion by applying pressure/vacuum in each chamber. This ability of the

IntelliPad is utilized to regulate the pressure at the skin-pad interface which is due to its three chambers' novel design and geometry.

Figure 3

IntelliPad's Structure

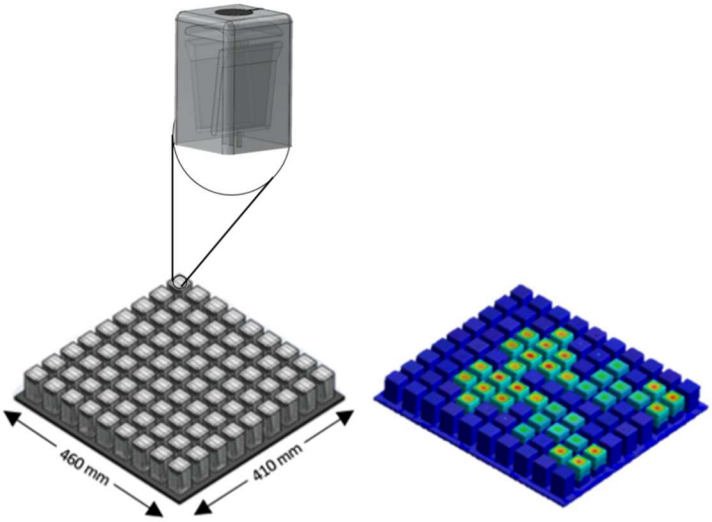

Note. (a) IntelliPad's deformation, based on the pressure distribution. (b) Schematic view of the IntelliPad [29].

2.1.1. *Design Requirements*

With regards to the maximum shear and normal stresses in two tissue locations (under-thigh and buttock) reported in [78], we measured the corresponding shear and normal displacements needed for each actuator to regulate the mentioned stresses. To measure this, skin tissue was assumed to be incompressible linearly-elastic material, possessing 0.15 MPa Young's modulus, 0.46 Poisson's ratio, and an average of 1100

kg/m^3 density. Using the maximum amount of shear stress as 0.3 MPa as described in [78] and assuming 0.5 for the coefficient of friction, we can determine the maximum amount of displacement (D) that is needed for the actuator to move horizontally to regulate this stress. Since the amount of the tissue deformation is small we assumed the following equations for computing the corresponding displacements:

$$G=E/(2(1+\nu)) \quad (1)$$

$$\gamma=\tau/G \quad (2)$$

$$D=\gamma t \quad (3)$$

Where G corresponds to the shear modulus of the tissue, E is Young's modulus, and ν Poisson's ratio of the skin tissue [78]. γ and τ are the shear strain and shear stress applied to the tissue and D and t are the shear displacement and thickness of the tissue respectively. Following the approach in [75], we consider weights of the subjects as 67 ± 9.6 kg, and the average thickness for the tissue overlying the sacrum, right and left ischial tuberosity, and the muscle thickness under femur as 13.8 ± 5.0 mm, 43.8 ± 5.4 mm, 43.0 ± 5.0 mm, and 27.05 mm, respectively from [84]. The calculated values for tissue shear displacements are listed in Table 1. In this study, the maximum value was taken as the guidance for design variables.

Table 1

Calculated Shear Displacements of Different Tissue Locations

Location	**T (Pa)**	**G (Pa)**	**ɣ (/)**	**t (mm)**	**D (mm)**
Ischial tuberosity	5700	51370	0.11	13.8	1.53
sacrum	5700	51370	0.11	43.0	4.77
Femur	5700	51370	0.11	43.8	4.86

Note. This was used as guidance for the actuator's design.

To measure the amount of normal pressure applied to the surface of each actuator, there is a force-sensitive resistor integrated on top of them (FSR) (Walfront, China). ISO standard 16840-2:2007 for the characteristics of the seating cushion was used as the size guide for the overall size of the pad [78]. Based on this we designed the IntelliPad with an overall size of 460 × 410 mm, (length × width).

The main goal of this study was to design an actuator that can achieve both horizontal and vertical motions independently. This was achieved by integrating three different individual chambers in each actuator. If the pressure applied to each chamber is controlled simultaneously we can achieve the desired motion. It is possible to achieve vertical motion by applying either pressure or vacuum to the top chamber. The top chamber has been designed to achieve maximum vertical motion while withstanding the required load on the top surface, produced by humans' weight. There is a V-shaped component integrated into the middle of two side chambers to pursue two main goals. This V-shaped structure is a weight-bearing structure as well as providing horizontal

displacement when on the opposite sides of the actuator, pressure and vacuum are applied concurrently.

Figure 4

Structure of A Soft Actuator

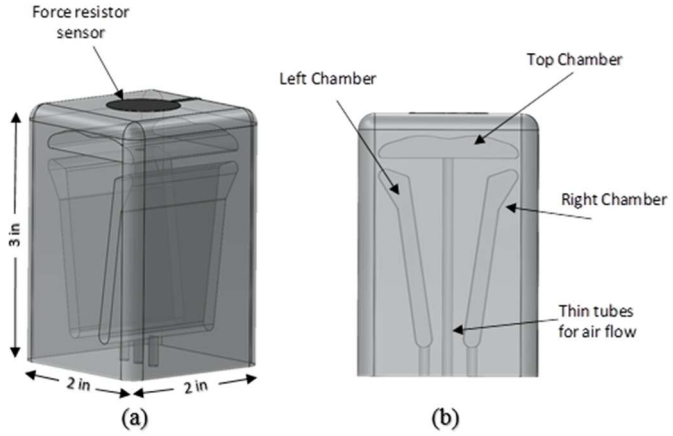

Note. The structure of the three air chambers and the sensor integrated on top is shown in both (a) orthogonal and (b) front views of the actuator [29].

This novel design was first sketched and modeled in computer-aided design software (SolidWorks 2016 x64 Edition). Each actuator's dimensions were specifically chosen with regards to the size of the overall pad; see Figure 3. Considering the overall size of the pad and the amount of pressure that each actuator was supposed to withstand, we reached the corresponding design shown in Figure 4. This design was first optimized iteratively using SolidWorks and FE computational solver ANSYS™Workbench. Utilizing the FE solvers, the design topology of each actuator was optimized manually

using SolidWorks and validating the new design with FE computational solver. This procedure was repeated several times until the desired displacement was achieved.

The optimization was first initiated considering only the side chambers aiming to reach the maximum horizontal displacement. After reaching the design configuration of the side chambers that satisfied the required horizontal displacements, the top chamber was added to allow regulating the upward and downward motions for regulating the normal interface pressure. The overall three-chamber layout design was further tested using structural FE analysis to optimize the thickness, location, size of each chamber, and size of the support structure. The iterative design evolution is depicted in Figure 5.

Figure 5

Empirical Design Optimization of The Actuator [29]

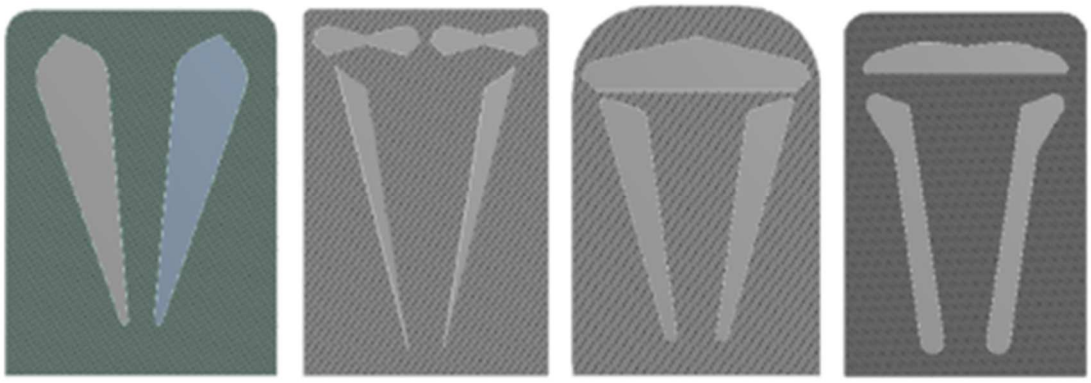

To improve the empirical design of the actuators aiming for further improvements of their mechanical performance a design optimization scheme was formulated. To reach the desired chamber layout and geometry rigorous design optimization methods were applied to the designed formulation scheme. This was not possible to achieve using

empirical methods or simple optimization modeling approaches, and resulted in a Non-Linear programming optimization approach which is defined in detail in Chapter 5. The geometry of each chamber was optimized using a finite element environment and analytical modeling in Deep Reinforcement Learning and Firefly Algorithm scheme design optimizations.

Considering only the cross-section of the actuator, the model was transformed into a 2D representation from a 3D framework. Symmetry is assumed for the x-y plane as it is demonstrated in Figure 6. The top chamber was neglected in this analysis so that only the horizontal motion of the actuator would be analyzed. The actuator was modeled as the combination of three beams connected by two virtual spring elements. In this model, the geometry of both outer beams is the same as is illustrated in Figures 6 e and g.

This model is also symmetric along the y-z plane, about the center of the cantilever placed in the middle. Cantilevers are modeled using the Euler-Bernoulli beam theory considering varying cross-sections for each one. To derive the analytical model for the actuator the modeling and formulation of tapered and thickened beams displacement were extended from [85]. This was possible with regards to the principle of superposition of displacements by connecting the beams with springs in between.

Figure 6

Model Representation of the Original Actuator Using Three Cantilever Beams and Virtual Springs Connecting Beams

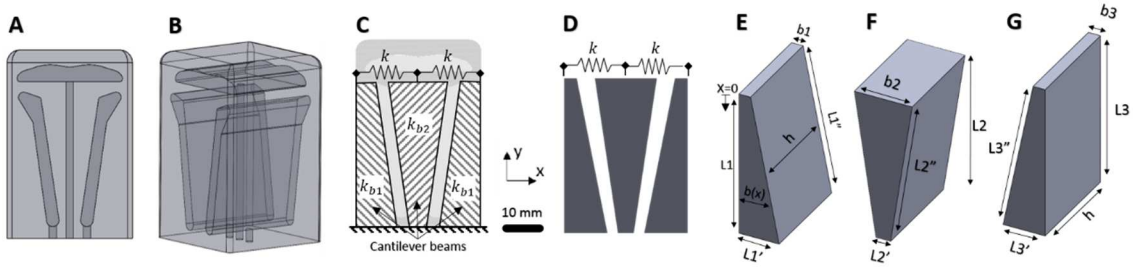

Note. (a) Front view, (b) Isometric view. (c) Actuator's model framing names the convection of each cantilever beam. (d) Cantilever model considering the virtual springs. Schematics of (e) first cantilever, (f) Second cantilever, (g) Third cantilever [30].

To demonstrate a multi-chamber composition performing as a soft pneumatic actuator, an analytical modeling approach was extended concerning the consideration of thickened and tapered beams. Due to the increased number of design space variables in the FE computational framework, the results of analytical models were later compared to finite element analysis for validation. Using the Euler-Bernoulli beam theory equations of displacement for each beam were derived individually. Considering the distributed loading along the length of each beam and the correspondent displacement derived from Euler-Bernoulli beam theory, and using Hooke's law the correspondent stiffness of each cantilever beam was derived.

2.2. Analytical Beam Model

A common definition of the beam-like structures stands for a structure possessing a much larger magnitude in one of its dimensions compared to the two other ones. The axis of the beam would be defined along with the larger one [86]. There are three main assumptions regarding Euler-Bernoulli beam theory as following:

Assumption 1: Infinitely rigid cross-section in its plane.

Assumption 2: After deformation, the cross-section of the beam remains plane.

Assumption 3: The deformed axis of the beam remains perpendicular to the cross-section after deformation [86].

In this classical model of beam theory, the effect of the transverse shear deformation is neglected. This assumption is only suitable for long beams. The more accurate method derived for larger beam deflections is the Timoshenko method, which is the modified version of the Euler-Bernoulli beam theory. In the Timoshenko method, the effect of transverse shear is also considered, which allows for a more accurate representation of beam deflections. Despite our actuator being made out of soft, hyperelastic material that can undergo large deformations, the Euler-Bernoulli beam theory was used to model our system, due to the goal of the study being to create a simple method with a sufficient approximation. Simplicity of the proposed modeling method was an important concern of this work to allow the use of this modeling approach in other soft robotic optimization applications. The derivations of the Euler-Bernoulli cantilever beam with applied distributed load is defined as

$$\frac{d^2\left(EI_{zz}(x)\left(\frac{d\Phi}{dx}\right)\right)}{dx^2} = q(x) \tag{4}$$

where $I_{zz}(x)$ represents the second moment of inertia through the z-axis and is changing concerning x, E is the Young's modulus, $q(x)$ is the applied distributed load on each beam, and Φ is the cross-section's slope which in Euler-Bernoulli beam theory is defined as $\frac{dy}{dx} = \Phi$.

The solution of tapered beam deflections is obtained by superposition of homogenous and particular solutions of (4) denoted by subscripts h and p, respectively, and is defined as:

$$\begin{aligned} y_i(x) &= y_h + y_p \\ &= C_1 + C_2 \ln(\alpha_i x + b_i) + C_3(\alpha_i x + b_i) + \frac{C_4}{\alpha_i x + b_i} \\ &\quad + \frac{3q_i}{2{\alpha_i}^4 Eh} \ln(\alpha_i x + b_i)(\alpha_i x + b_i) \end{aligned} \tag{5}$$

Figure 7

Cantilever Beam Model Parameters and Coordinates

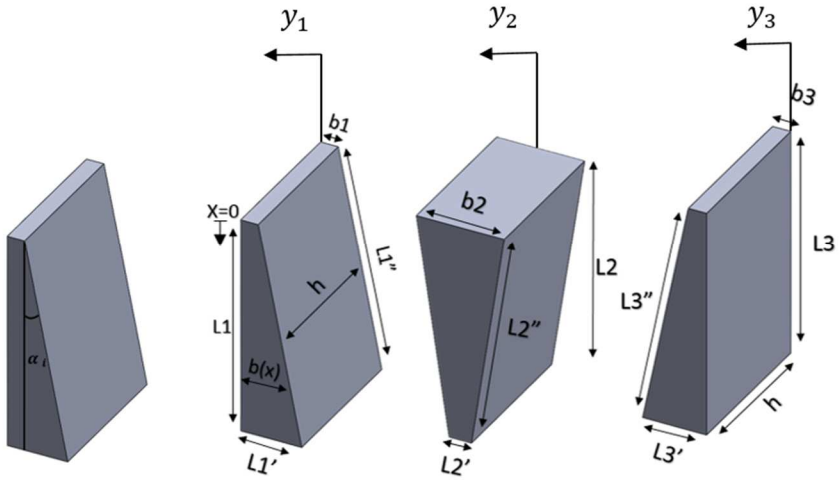

where α_i is the slope of the tapered or thickened beams for i – th beam shown in Figure 7, q_i is the distributed load applied to each beam due to vacuum/pressure in the individual air chambers, E is the young's modulus of the material which is elaborated more in the upcoming sections, b_i is the thickness of the tapered beam and the thickened cantilever at x=0, and h is the air chamber's width. Along the length of each beam is applied a distributed loading (i.e., internal pressure/vacuum inside chambers) and at the free tip of the beam, a concentrated loading due to a virtual spring is applied. Considering the loading and boundary conditions we can solve for the constants C_1, C_2, C_3, and C_4 by differentiating (5) and solving for the boundary conditions. The set of equations from differentiation of (5) and boundary conditions are defined as

$$\frac{dy}{dx} = \frac{C_2}{\alpha_i x + b_i} + C_3\alpha_i - \frac{C_4}{(\alpha_i x + b_i)^2} + \frac{3q_i\alpha}{2{\alpha_i}^4 Eh}[\ln(\alpha_i x + b_i) + 1] \quad (6)$$

$$\frac{d^2y}{dx^2} = -\frac{C_2\alpha_i}{(\alpha_i x + b_i)^2} + \frac{2{\alpha_i}^2 C_4}{(\alpha_i x + b_i)^3} + \frac{3q_i}{2{\alpha_i}^2 Eh(\alpha_i x + b_i)} \quad (7)$$

$$\frac{d^3y}{dx^3} = \frac{2{\alpha_i}^2 C_2}{(\alpha_i x + b_i)^3} - \frac{6{\alpha_i}^3 C_4}{(\alpha_i x + b_i)^4} - \frac{3q_i{\alpha_i}^2}{2{\alpha_i}^3 Eh(\alpha_i x + b_i)^2} \quad (8)$$

$$M = EI_{zz}\left(\frac{d^2y}{dx^2}\right) \qquad M(0) = 0 \quad (9)$$

$$E\frac{dI_{zz}}{dx}\left(\frac{d^2y}{dx^2}\right) + EI_{zz}\left(\frac{d^3y}{dx^3}\right) = \upsilon + \frac{d\mu}{dx} \quad \upsilon(0) = 0 \quad (10)$$

where $M(x)$ is the moment of inertia along each beam with x=0 defined at the free tip of the beam, and $\upsilon(x)$ is the corresponding shear force. The functionality of the thin elastic material that forms a closed chamber with the combination of the beams is taken into account in the formulations and analytical models as virtual springs.

Application of the boundary conditions leads to a solution for the constants defined as

$$C_1 = -C_2 \ln(L_1') - C_3(L_1') - \frac{C_4}{L_1'} - \frac{3q_i}{2{\alpha_i}^4 Eh} \ln(L_1')L_1' \tag{11}$$

$$C_2 = \frac{3q_i b_i}{{\alpha_i}^4 Eh} \tag{12}$$

$$C_3 = \frac{C_4}{(L_1')^2} - \frac{C_2}{\alpha_i L_1'} - \frac{3q_i}{2{\alpha_i}^4 Eh} [\alpha_i \ln(L_1') + 1] \tag{13}$$

$$C_4 = \frac{3q_i \alpha_i b_i^2}{4{\alpha_i}^4 Eh} \tag{14}$$

2.3. Governing Equations of Motion

Considering the derivation of deflection of an individual cantilever beam in the previous section and using the principle of superposition for the distributed loading applied to each beam through the virtual springs on each free tip of the beams (x=0) as concentrated loading, we can derive the equations of motion for the overall deflections of all three beams (y_{0_1}, y_{0_2}, y_{0_3}) as follows.

$$y_{0_1} = \frac{y_1 - y_{0_2}(k_s/k_{b_1})}{(1 + k_s/k_{b_1})} \tag{15}$$

$$y_{0_2} = \frac{y_2 - y_1 + \frac{(k_s/k_{b_1})y_{p_1}}{(1 + k_s/k_{b_1})} - y_3 \frac{k_s k_{b_3}}{k_{b_2}(k_{b_3} + k_s)}}{1 - \frac{k_s^2 k_{b_3}}{k_{b_3} k_{b_2}(k_{b_3} + k_s)} - \frac{k_s^2}{k_{b_2}(k_{b_1} + k_s)} + \frac{2k_s}{k_{b_2}}} \tag{16}$$

$$y_{0_3} = \frac{(k_s/k_{b_3})y_{0_2} - y_3}{(1 + k_s/k_{b_3})} \tag{17}$$

The stiffness of each virtual spring which resembles the material between each cantilever is defined as k_s. Each cantilever's effective bending stiffness is represented as k_{b_i}, for the *i*-th beam, where *i*=1, 2, 3. To optimize each chamber's geometry the set of equations (15-17) is used. Two different optimization methods were utilized to reach the maximum horizontal displacement concerning a constant amount of pressure applied into each chamber. In the following section manufacturing process of the actuator and the corresponding material, characterization is presented.

Chapter 3

Fabrication and Material Characterization

Making any soft robot design come to reality is not possible without using fabrication tools. There are various existing methods for the fabrication of soft robots. Casting and molding are the common techniques used amongst soft robotic societies for fabricating and creating single-material soft systems [87]. Fabrication and casting of soft actuators and systems possessing complex inner geometries, higher degrees of freedom, or multi-material are possible with fused-deposition-model-based techniques using 3D printers [88]. The molding approach, a common method for the fabrication of soft robotic actuators [29], has been used in this study to create each actuator.

3.1. Multi-Stage Molding Process

A multi-step molding approach was used to manufacture each actuator. The material used to make the molds was Polylactic acid. Each mold was created using 3D printers. The molds were a combination of multi-part male and female pieces which were precisely designed to create the air chambers and also to ease the unmolding process. First, a silicone rubber (EZ-M25, EZ Sil, Oakland, CA) was selected due to its favorable chemical (i.e., inert) and mechanical (i.e., hardness and strength) material properties. This material satisfied the required criteria to be used for direct skin interactions as well as being easy to clean and maintain. Silicone rubber materials are mainly easy to fabricate and manufactured and this particular material had the desired hardness for tolerating our required load-bearing capabilities. This material was composed of two separate materials in a liquid phase, which were supposed to be mixed with a 1:1 mixing ratio before pouring into the molds. The required time for the material to be cured was between 4-5

hours. To allow supplying pressure/vacuum to each chamber, 3 mm tubes were inserted in the embedded holes in each actuator. The silicone tubes were specifically chosen for the required task, due to their elastic material properties being similar to the actuator's material. The reason for this was to avoid any unwanted or unexpected effects due to different material stiffness of tubes affecting the actuator's movement and its structure.

Figure 8

Materials Used in Fabrication of IntelliPad

(a) (b)

Note. (a) EZ-M25, EZ Sil, Material which was used in the first trial [29, 89], (b) Elite Double 22, Zhermack, the second material used in the optimization process of each actuator [30, 90].

Due to the fabrication limitations using EZ-M25 material (i.e., difficulties with improper curing and longer than desired curing times) a different silicone rubber was

later used to fabricate soft actuators. A silicone rubber (Elite Double 22, Zhermack, Badia Polesine, Italy) was selected due to the ease of manufacturing, being safe for skin/tissue contact, and reduced amount of curing time, which allows for the fabrication of more actuators in a shorter time. The hardness of the second material was slightly lower (Shore A 22 compared to previous Shore A 25), which led to the increased amount of displacement while still having enough amount of load-bearing. The specific advantages of the Elite Double 22 over the EZ-M25 are higher dimensional stability over time, a much faster curing process, high elastic recovery, and high fluidity. High fluidity allows mixing two parts of the material without requiring to use vacuum for degassing to eliminate any bubbles formed during the mixing process. This simplifies the fabrication process of the material and the quality of the end product.

Figure 9

The Fabrication Process of Each Actuator

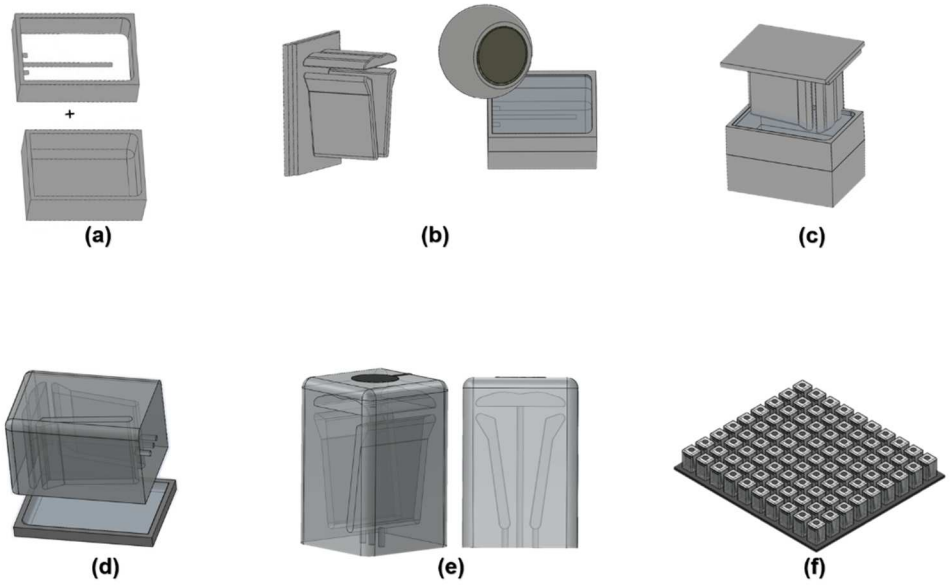

Note. The fabrication process by which each actuator was constructed, was the same for both materials. (a) Assembly of the multipart mold. (b) Casting the silicone rubber in a prepared female mold. (c) Inserting the male mold to create air chambers. (d) Pouring silicone in a flat mold and placing the cured silicone part on top of that to seal the inner chambers. (e) Placing a force sensitive resistor on top of the actuator. (f) IntelliPad structure as proposed in [29].

3.2. Material Description

EZ-M25, EZ Sil: The hardness of the EZ-M25 silicone rubber is Shore A 25. This material is liquid at room temperature, with two components, part A and part B. It takes between 4-5 hours to cure after mixing both parts A and B with a mixing ratio of 1:1. Its viscosity is 3000 cps. It has a translucent color. Non-stick, food-grade silicone

rubber is nontoxic, odorless, environmentally friendly, and resistant to high temperatures. This material stays intact for a long period and is resistant to aging. Most importantly this material has a high tear strength, which makes it a suitable material for wearing and shearing [89].

Elite Double 22, Zhermack: The Elite Double 22 silicone rubber with two parts A and B has a mixing ratio of 1:1, with a Shore hardness of A 22. It has a tensile strength of 2.5 MPa. The material's elongation at break is 550%, its resistance to tearing is 5 MPa. It is extremely fluidic, odorless, color is green, and is primarily used in dental applications, which makes it compatible with medical applications.

Both material's computational and constitutive models are explained in the following chapter.

3.3. Computational and Constitutive Material Model

3.3.1. *Material Characterization*

The selected EZ-M25 silicone material's mechanical properties were characterized and tested according to the ASTM D638 standard which supports using digital image correlation (DIC) for stress-strain characterization. Dog-bone shape samples of this material were made and tested using a universal testing machine (Shimadzu AGS-X 10kN, Columbia, MD), shown in Figure 10. The digital image correlation (DIC) method was used for more accurate results. To facilitate the DIC, a high-contrast coating layer including random speckles was used on the surface of the dog-bone sample. A biaxial tensile test's loading was performed on the sample through the y-axis. Strain components

were measured in x and y directions. The values of 0.3988 and 0.657 MPa were calculated for Poisson's ratio and Elastic Modulus, respectively.

Figure 10

Schematics and Examples of Material Samples Used in Material Characterization

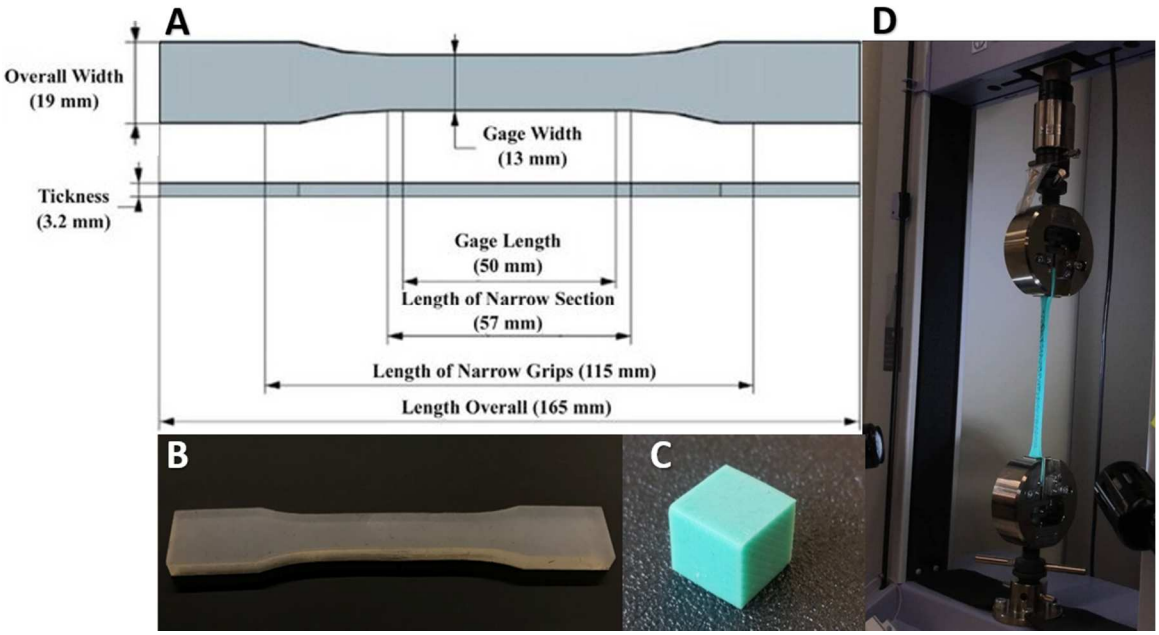

Note. (A) ASTM D638 standard size guideline [91]. (B) Dog-bone sample fabricated from EZ-M25 silicone rubber used for the tensile test. (C) Material sample fabricated from Elite Double 22 silicone rubber used for the compression test. (D) Dog-bone sample fabricated from Elite Double 22 silicone rubber under the stress-strain test in the universal testing machine.

Since the selected EZ-M25 silicone material has a positive Poisson's ratio and behaves in a hyperelastic manner when it undergoes large amounts of strain, the thickness

of the material, including the part hold by the grippers, decreases. This makes the material prone to slipping from the gripper during testing. To eliminate this issue, various methods were applied, including continuously tightening the grippers. However, this resulted in the curve fluctuating. If the effect of this unwanted fluctuation is being disregarded, the overall stress-strain curve including at large strains (200%) shows to be linear, see Figure 11 (A). Precise stress-strain characterization within a smaller strain rage was achieved using DIC, showing nearly linear behavior. Considering this, we assumed a linear behavior for silicone rubber (EZ-M25, EZ Sil). Based on the preliminary FE simulation results (discussed in later Chapters), the maximum expected principal strain was determined to be 80%. Therefore, a strain rate of lower than 200% was provided in the stress-strain curve of the silicone rubber material. To measure the results of the stress-strain curve of this material more accurately, Digital Image Correlation (DIC) method was utilized, which is illustrated in Figure 11 (B). When using DIC, the camera is static with a fixed field of view that limits the measured strain range. This led to measuring the strain ranges of the silicone material to be lower than 20%. Since we assumed a linear behavior for this silicone material we derived Young's modulus and Poisson's ratio from the DIC method for more accurate results.

Figure 11

Strain-Stress Curves of the Silicone Rubber (EZ-M25, EZ Sil)

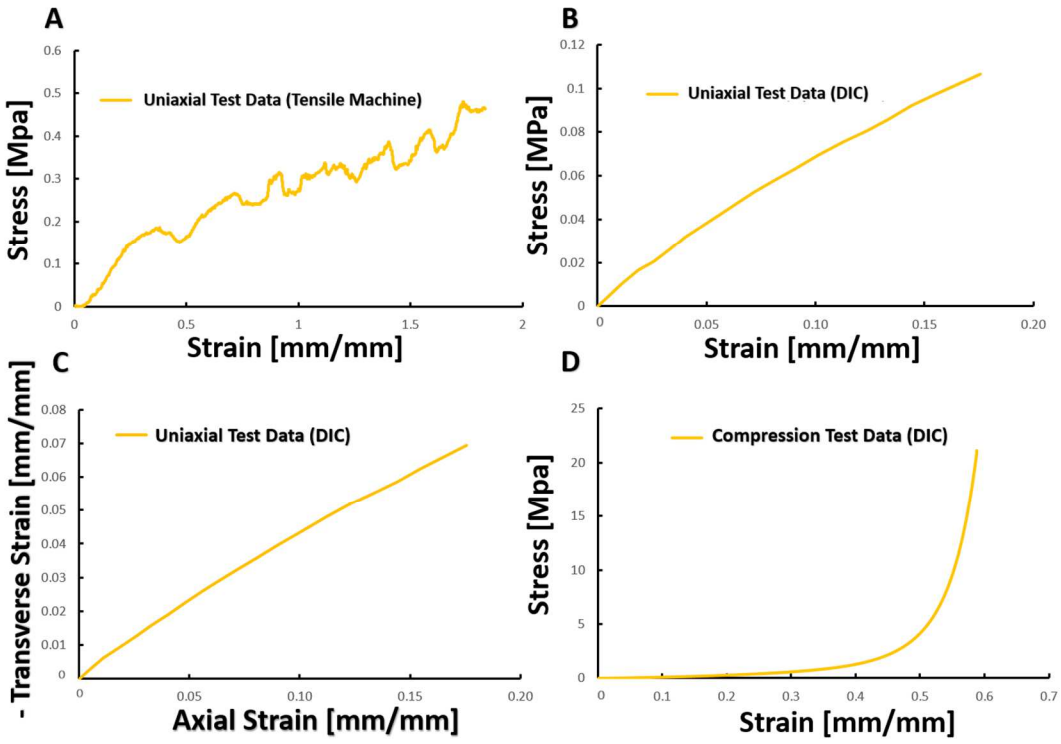

Note. The results of experimental material characterization of the silicone rubber (EZ-M25, EZ Sil, Oakland, CA). A, Experimental testing data using B, universal testing machine (Shimadzu AGS-X 10kN, Columbia, MD) for strain range of < 2, and (b) using DIC approach for strain range of < 0.2. C, Uniaxial experimental Transverse and Axial strain test data. D, Uniaxial compression test data using DIC.

$$\nu = \frac{-d\varepsilon_{Transverse}}{d\varepsilon_{Axial}} \tag{18}$$

Using the corresponding test data, the Young's Modulus of the material which is equal to the slope of the curve in Figure 11 (b) was 0.657 MPa. Employing the data measured experimentally with DIC, transverse and axial strain amounts were measured, see Figure 11 (c). Considering the corresponding data and Eq. (18), Poisson's ratio of the material was calculated from the measurements.

The same process was utilized for the selected silicone rubber (Elite Double 22, Zhermack, Badia Polesine, Italy). Mechanical properties of this material were derived to be used as an input to the FE computational model. For this particular material, both uniaxial tensile and compression tests were performed to obtain the hyperelastic material model parameters. To obtain the best curve fit of the silicone rubber a compression test was also utilized using DIC method, see Figure 11 (D).

The main goal of the material characterization of the tensile test was to determine suitable strain energy functions for each material. To evaluate the desired functions uniaxial tension and compression tests were performed.

3.4. Material Model Characterization

Rubber and rubber-like materials, which are common hyperelastic materials used in various industry applications can return to their initial form while experiencing large deformations under small loads. Since hyperelastic material's stress-strain energy is highly non-linear, to characterize their behavior it is not enough to describe it with only a modulus of elasticity [92].

The strain energy function and the behavior of the hyperelastic material are derived based on three strain invariants I_1, I_2, and I_3. The strain energy function of the

material is the energy stored per unit volume of the material when it is in its initial shape and before it goes through deformation at one specific point in the material [93]. The strain energy function W and the three invariants are defined as:

$$W = f(I_1, I_2, I_3) \tag{19}$$

$$I_1 = \boldsymbol{\lambda}_1^{\,2} + \boldsymbol{\lambda}_2^{\,2} + \boldsymbol{\lambda}_3^{\,2} \tag{20}$$

$$I_2 = \boldsymbol{\lambda}_1^{\,2}\boldsymbol{\lambda}_2^{\,2} + \boldsymbol{\lambda}_2^{\,2}\boldsymbol{\lambda}_3^{\,2} + \boldsymbol{\lambda}_3^{\,2}\boldsymbol{\lambda}_1^{\,2} \tag{21}$$

$$I_3 = \boldsymbol{\lambda}_1^{\,2}\boldsymbol{\lambda}_2^{\,2}\boldsymbol{\lambda}_3^{\,2} \tag{22}$$

where $\boldsymbol{\lambda}_i$, (i=1,2,3) are the principal stretch ratios of the material. The stretch ratios of the material are defined as the proportion of the length of the deformed line element over the length of the corresponding line element in the undeformed state.

$$\boldsymbol{\lambda}_i = \frac{|dx|}{|dX|} \tag{23}$$

If the material is incompressible $I_3 = 1$; this makes the strain energy function of the material to be only a function of I_1 and I_2 [94].

$$W = W(I_1 - 3, I_2 - 3) \quad (24)$$

There are two main different ways material models are defined in ANSYS. Both describe strain energy function but in different ways. One describes it from the perspective of continuum mechanics and is the phenomenological model. The other describes it from the perspective of microstructure [92]. In this study, material models are described using continuum mechanics solutions of ANSYS. Several hyperelastic material models were developed and are explained here for completeness.

3.4.1. *Mooney-Rivlin Model*

This hyperelastic material model employs two parameters to define large strains in shear and uniaxial deformations. However, this model is unable to represent the upturn in the uniaxial test's force-extension and shear test's force-shear displacement [51, 95].

$$W = C_{10}\,(I_1 - 3) + C_{01}\,(I_2 - 3) + \frac{1}{D_1}\,(J_{el} - 1)^2 \quad (25)$$

3.4.2. *Neo-Hookean Model*

Neo-Hookean model as well as the Mooney-Rivlin model cannot capture the upturn (S-Curvature). This model is a special case of the Mooney-Rivlin model in which $C_{01} = 0$. However, this model is a useful method when data is insufficient and it provides good estimation at relatively small strains [92].

$$W=C_{10}\ (I_1-3)+\frac{1}{D_1}(J_{el}-1)^2 \tag{26}$$

3.4.3. *Full Polynomial Model*

The material being isotropic and compressible are two main assumptions for the Polynomial model which is given by:

$$\mathrm{W}=\sum_{ij=0}^{3} C_{ij}(I_1-3)^i(I_2-3)^j+\sum_{ij=0}^{3}\frac{1}{D_i}(J_{el}-1)^{2i} \tag{27}$$

In this model, C_{ij} represents one of the material constants that the shear behavior of the material depends on it and it can be measured from uniaxial, biaxial, and planar tests. D_i is one of the other material constants that the bulk compressibility is dependent on it and is equal to zero if the material is completely incompressible. This can be measured through the volumetric test. J_{el} is the elastic volume ratio of the material, and N denotes the number of terms in the strain energy function [92].

3.4.4. *Reduced Polynomial Model*

The material model does not depend on the invariant I_2. The sensitivity of the model on I_1 is much more than I_2. If the test data is limited it is suggested that

eliminating I_2 would improve the results [92, 96]. An example of the first-order reduced polynomial model is the Neo-Hookean model [92].

3.4.5. *Yeoh Model*

Yeoh model is based on only invariant I_1. This model is in the third-order polynomial form and it is a phenomenological model. Unlike Mooney-Rivlin and Neo-Hookean models, this one can present the stress-strain curve's upturn [92, 97]. This model gives a good approximation for the large strains with limited data. The reduced polynomial model is another way of calling the Yeoh model. For compressible hyperelastic materials this model is represented as:

$$\mathrm{W} = \sum_{i=1}^{3} C_{i0}(I_1 - 3)^i + \sum_{i=1}^{3} \frac{1}{D_i}(J_{el} - 1)^{2i} \tag{28}$$

3.4.6. *Ogden Model*

This phenomenological model of deriving the strain energy function relies on using the principle stretches instead of invariants. This model can represent upturn similarly to the Yeoh model. The accuracy of this model for large ranges of deformation is high. Unlike the Yeoh model, this model cannot analyze different modes of deformation with limited data [50, 92].

$$W = \sum_{i=1}^{N} \frac{2\mu_i}{{\alpha_i}^2}\left({\boldsymbol{\lambda}_1}^{\alpha_i} + {\boldsymbol{\lambda}_2}^{\alpha_i} + {\boldsymbol{\lambda}_3}^{\alpha_i} - 3\right) + \sum_{i=1}^{N} \frac{1}{D_i}(J_{el} - 1)^{2i} \tag{29}$$

3.4.7. *Experimental Material Characterization*

The non-linear hyperelastic behavior of the materials used in this study was tested experimentally and modeled as the Ogden model, described by the strain energy function as in (29). Using the sample's test data, material parameters were obtained. Considering the incompressibility of the silicone rubber material [98], the first-order Ogden model was selected for the nominal strain of lower than 1.2 to fit the correspondent data.

Figure 12

Hyperelastic Material Model Fit of Experimental Material Characterization Results

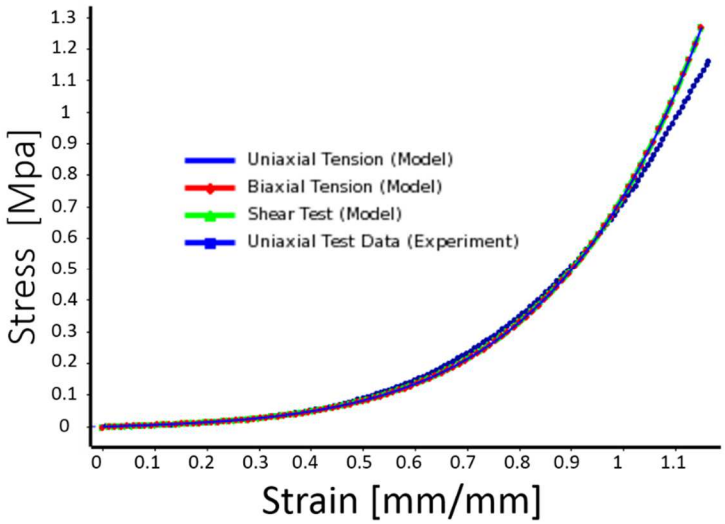

Note. This model was best fitted with the first-order Ogden model. The maximal principal strain of the actuator at maximum applied vacuum/pressure in air chambers is less than 0.5 and model strains less than 1.1 have been considered.

Coefficients of this material model were measured as α_1=2.4914, μ_1= 45480, and D_1=0, where D_1 is the incompressibility parameter. The data derived from the sample was input into the Finite Element Analysis ANSYS workbench software. The actuator was modeled in a way to support large strain hyperelasticity utilizing higher-order 20-node SOLID186 and higher-order 10-node SOLID187 elements. In the next chapter, optimization methods used in this study to optimize the chambers designs are provided and explained in detail.

Chapter 4

Optimization Methods

4.1. Introduction to Optimization

The optimization process is deeply engrained at the heart of many engineering applications. Over the years, many optimization methods have been developed and various associated cost functions have been proposed. Broadly, one may consider that the optimization process decomposes into linear and nonlinear problems that can address convex and nonconvex functions, respectively. However, a rich dichotomy exists between methods that comprise the associated subsets of methods.

Convex functions are extensively encountered in optimization and should dictate one's choice in a suitable programming method. Convexity can be graphically assessed by drawing a secant line between two points and determining if the function f(x) is below the line for a univariate case [99]. When considering a multivariate case then the Hessian matrix will provide the necessary information. Namely, if the Hessian is positive semidefinite the function has a strong local minimum and is convex [100]. In short, if a local minimum is a global minimum the criteria are met. For these functions, simple linear programming and gradient-based descent are easily scalable for a solution.

Non-convexities offer several challenges to their convex counterparts and may encourage the use of nonlinear optimization and more advanced methods that inject some randomness to achieve global minimum or maximum [99]. Such problems can have multiple extrema, saddle points, or very large regions with zero slopes. In these applications, gradient approaches can fail due to becoming stuck at local extrema,

however, evolutionary and swarm-based methods are examples of methods that are suitable for such analysis.

4.2. Cost Function and Method Selection

The analytical model derived in Chapter 3 is used herein to construct a cost function for the air chamber shape optimization. For this work, the deflection of the tip of the leftmost/outer cantilever is considered for optimization. This is intended to reflect the horizontal motion across the bulk of the top of the surface of the actuator that is intended to be maximized. An inherent disadvantage of the model is that it cannot predict contact interactions. Furthermore, in both FE simulations and experiments presented in the upcoming sections it was discovered that to prevent cantilever beams to bend and make a bubble-type of motion, the deflections about the midpoints of the rightmost and central (see Figure 7) cantilevers need to be minimized. The assumption is that if the beams are in contact then they have achieved maximal in-axis displacement. This is the reason for defining parameters d_1 and d_1'. Where d_1 is the distance between both the first and the second cantilevers and the third and the second cantilevers at x=0 and d_1' is the same distance but at $x = L_1$. Equation 30 presents the cost function considered and the optimization problem is defined as

$$minimze \quad -Y_{0_1} + Y_{0_{2_{mid}}} + Y_{0_{3_{mid}}} \tag{30}$$

$$subject\ to\ \left(Y_{0_1} - b_1\right) + \left(Y_{0_2} + \frac{b_2}{2}\right) - d_1 = 0 \tag{31}$$

$$b_1 + b_2 + L_2' - 0.03 > 0 \tag{32}$$

$$b_1 + b_2 + b_3 + d_1 - 0.0508 < 0 \tag{33}$$

$$L_1' + L_2' + L_3' + d_1' - 0.0508 < 0 \tag{34}$$

$$0.1 < \frac{L_2'}{b_2} < 0.9 \tag{35}$$

$$0.1 < \frac{b_1}{L_1'} < 0.9 \tag{36}$$

$$0.1 < \frac{b_3}{L_3'} < 0.9 \tag{37}$$

Where all geometric parameters L_i, L'_i, b_i, and b'_i, for the *i*-th beam, with *i=1-3*, are referenced from Figure 7 and are associated with the chamber geometries. $Y_{0_{2_{mid}}}$ and

$Y_{0_{3_{mid}}}$ stand for the deflection of the second and third beam at $x = \frac{L_1}{2}$ respectively which is the midpoint of each cantilever. The main reason for defining this was to inhibit each cantilever to bend and create a bubble-shaped motion. In the sequential order, the first constraint (Eq. 30) states that considering symmetry and the applied vacuum, the amount of the first cantilever's displacement subtracted by the size of its top portion (b_1) and the amount of the second cantilever's displacement and added half of the size of its top portion, cannot exceed the size of the virtual spring between them which is defined by d_1. In other words, the overall deflection of the first and the second cantilever must equal to $d_1 + b_1 + \frac{b_2}{2}$. The second constraint (Eq. 31) enforces that the minimum thickness required for one single cantilever to withstand the normal load applied on top of the actuator due to human weight is 0.03 m. Therefore, the summation of the three cantilevers smallest portions cannot be less than 0.03 m. Similar criteria are present for the third and fourth constraints. The final three constraints ensure that chamber optimization routines do not select square topologies which would lead to undefined $\alpha_n$values per equations 35 to 37.

Parameters d_1 and $d_1'$are defined as

$$d_1 = 0.0548 - (2b_1 + b_2) \tag{38}$$

$$d_1' = 0.0548 - (2L_1' + L_2') \tag{39}$$

4.2.1. *Penalty Function*

Constrained optimization problems consider some functions subject to inequality and equality constraints. Removal of constraints will transform the problem to unconstrained [100]. From an implementation standpoint, especially for the non-linear programming problem, constraints can make the realization of the global minimum or maximum very challenging [101]. Considering that a nonlinear problem subjected to many constraints could be subject to several local minima imposed by the constraints, it is often advantageous to remove the constraints. Powell's method can be used to transform a constrained optimization problem into a series of unconstrained optimization problems [102]. This can be achieved using penalty function methods as presented in [101] and is referenced herein for the remainder of this subsection. Penalty functions are used to make a combination of constraints that minimize a cost function while penalizing the functions for misbehaving with penalty terms. This approach was used in our implementation of cost functions used in the following sections and is formally defined as [101]

$$Minimize\ f(x) + \mu\ maximum\{0|g(x)\} \tag{40}$$

$$subject\ to\ x \in R^n \quad [101] \tag{41}$$

4.2.2. *Cost Function Selection and Solution Space Manifold Visualization*

Before the selection of a suitable optimization algorithm, it is important to understand the parameterization of the optimization's solution space, usually laying on a surface or manifold, or its relative macroscale behavior. The presence of logarithmic terms and composition of trigonometric functions in equations 5 to 16, and respectively implies that the design space is highly non-linear with a plethora of non-convexities. In model-based optimization, the top and bottom dimensions of the actuators' cantilevers are considered optimization parameters. For ease of visualization of the solution space, their ratios are plotted concerning the modified cost function in equation 30 using Powell's method for transformation into an unconstrained problem.

Figure 13

Ratios of Chamber Parameter Vs. Cost

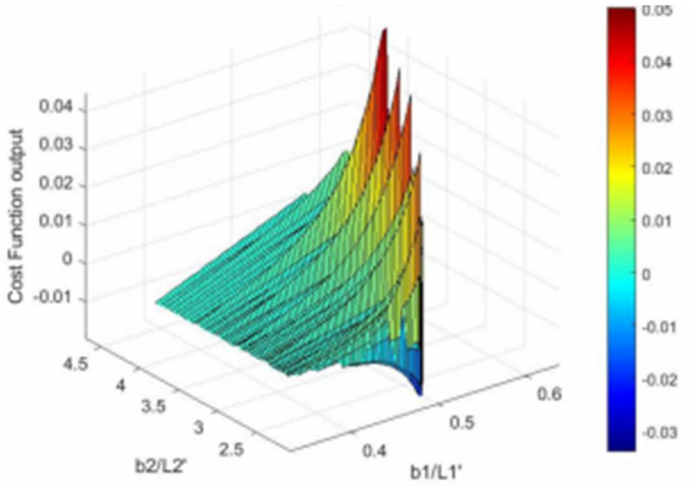

Note. The plot of the ratios of considered cantilever parameters to visualize non-convexities present in the surface that drive the selection of the optimization methods.

Given the notable peaks and valleys present in this solution space representation, gradient-based methods may not yield an optimal solution. Thus, non-linear and emerging techniques were used in this work.

4.3. Model-Based Firefly Optimization

Non-linear and highly non-convex optimization problems offer unparalleled challenges that classical linear-based methods such as Lagrange multipliers, Simplex methods, and other linear programming methods fall short on. The domain of nonlinear programming offers many attractive solutions, however, in the literature over the past two decades evolutionary and swarm intelligence methods have seen the spotlight. These

methods are well suited for handling problems with discontinuous and non-convex design spaces and have shown notable success where other non-linear programming methods have failed [100]. Applications-based work has shown that swarm intelligence methods are more accurate and robust than the genetic evolutionary algorithms, and herein the focus is to use swarm intelligence-based algorithms.

Swarm intelligence-based methods are examples of stochastic algorithms and are often constructed by a hybrid combination of a deterministic component and a random component that allows for a comprehensive exploration of space even in the presence of discontinuity or multiple extrema [103]. A large portion of these swarm intelligence-based methods classify as nature-inspired metaheuristic algorithms and are of increasing popularity. Some well-known examples include Firefly algorithm (FA), Cuckoo Search (CS), Ant Colony (AC), and classic particle swarm optimization (PSO). FA is by far one of the more popular algorithms and has been shown in comparative studies to perform very well compared to CS and PSO [65], therefore was selected as the optimization method for this work.

4.3.1. *FA Theory and Modification*

FA is based on the behaviors associated with bioluminescence in swarms of fireflies, where one firefly will be attracted to another concerning their attractiveness and brightness. The algorithm assumes that the flies are unisex and can attract any fly. Brightness and attractiveness are proportional, and the brightness is dependent on the cost function and can sometimes be proportional [103]. In this work, a modified FA algorithm is scripted, and further details of the algorithm are presented for the base algorithm and modified variant.

The base algorithm is herein referenced from [103] in its presentation. In the case of the base algorithm, the two most important factors are light intensity and attractiveness. Light intensity is expressed as

$$I = I_0 e^{-\gamma r} \tag{42}$$

where γ is a constant of proportionality known as the light absorption coefficient and is present from the base assumptions in the algorithm, I_0 is the base light intensity and is a user-defined hyper parameter, and *r* is defined as the distance between two fireflies and can be solved using a Cartesian norm [104]. The Cartesian norm between the position of the *i*-th firefly, x_i, and the position of the *j* -th firefly, x_j, is defined as

$$r = \left\| X_i - X_j \right\| \tag{43}$$

The attractiveness is defined as

$$\beta = \beta_0 e^{-\gamma r^2} \tag{44}$$

where the only new term is β_0 which defines a baseline attractiveness when their distance is zero. Algorithmically, fireflies populate the solution space in a stochastic

fashion. For a set number of iterations, for all dimensions, their relative light intensity is determined, and fireflies will attract the brighter ones and update all equations iteratively. Updates for the movements of the fireflies is given as [104].

$$X_i = X_i + \beta\left(X_j - X_i\right) + \alpha\varepsilon_i \tag{45}$$

To inject the stochastic element into the algorithm, ε_i samples a random variable and is multiplied by a mutation coefficient designated as α, where a damping coefficient for mutation is considered to help encourage sufficient exploration.

While the algorithm proposed by [103] is well documented to be extremely efficient, other works have offered improvements to the algorithm. Specifically, the implemented algorithm uses a memory mechanism as proposed in [104]. The overarching goal is to transfer information from generation to generation. The reason this is desirable is that in each generation fireflies approach an extremum on an optimization surface. However, in the next generation, its position is changed and information about its last position may be lost. Such a mechanism will allow for both exploration and exploitation in the optimization problem [104]. While many stochastic algorithms do have some mechanism of this form engrained, most swarm-intelligence methods do not [104]. In our work, we encode in the algorithm that some fireflies that are closer to optimal values are stored for the next generation. Algorithm 1 details the implementation of the modified FA program.

Algorithm 1: Implementation of modified FA program.

Initialize design parameters to be optimized (b1, b2, L1', L2')

Converged = 0

While Converged = 0 do

for i = 1 to maximum iteration

Feed into FA

Calculate displacement value from Model-Based Equations

Check the side constraints

Sort the fireflies based on the displacement values

Present the first firefly as the best solution obtained

end

end

4.3.2. *FA Simulations*

Using Algorithm 1, the modified FA program was coded in MATLAB (R2020a). This code is a hybrid of the base code from [105] and the amendments proposed by [104]. The swarm size is 25 fireflies that will exist throughout 50 generations with a light absorption coefficient ($\gamma = 1$), attraction coefficient base value ($\beta_0 = 2$), a mutation coefficient ($\alpha = 0.2$), and a mutation coefficient damping ratio of ($\alpha_{damp} = 0.98$). Results from this optimization are presented in Section 5.5 along with the comparison results obtained from a deep reinforcement learning-based approach presented in the next section.

4.4. Deep Reinforcement Learning-Based Shape Optimization

Machine learning has swiftly transformed several facets of engineering in recent years, including the field of soft robotics. To date, such methods have seen notable interest in improving sensory aspects of soft robotic systems; such as [106] where the authors used 3D convolutional neural networks (3D CNN) to improve the dexterity of PneuNet actuators for grasping tasks. There is also an increasing interest in control via reinforcement learning (RL). For example, studies in [103, 107] employ the use of RL for control of cuttlefish robots that use a dielectric elastomer-based actuation principle. Machine learning techniques are very well suited to soft robotics due to their capacity to deal with nonlinear environments and material behaviors. The most classic use case is in model-free control where an agent can learn bio-inspired imitation, manipulation, or navigation based on a reward signal [108].

Deep learning techniques are scalable to optimization problems for a labeled dataset; however, for design exploration of novel topologies unsupervised learning methods present a more attractive solution to best explore the environment and learn optimal shapes. Few studies have considered RL for shape and/or structural optimization; and in the soft robotics domain a recently published work performed by this research group exists [30] and is part of this thesis. The original inspiration for the use of deep RL-based optimization originates from [109], where the authors used RL for flow sculpting and design of microfluidic devices for the inverse physics problem. In another recent work, study in [110] used RL for the angle of attack optimization of an airfoil for a discrete action variable. The closely related work in[111] developed a single-step episode methodology for deep RL-based shape optimization. In this thesis, a similar approach is

used. The next subsection briefly discusses some of the underlying mechanisms of deep RL for the considered policy.

4.4.1. *Fundamentals of Deep RL and the Deep Deterministic Policy Gradient*

Machine learning can be broadly represented into three main categories: supervised learning, unsupervised learning, and reinforcement learning. Supervised learning is used when a labeled dataset is available and can be used for classification and regression problems. Unsupervised learning focuses more on pattern identification and outputting a protocol to complete a related task. Lastly, in reinforcement learning an agent interacts with an environment by acting while in a particular state. When the action is performed it is rewarded, and the process is iteratively repeated [112].

Before discussing the selected algorithm, some preliminaries must be presented to rationalize its selection. RL algorithms are generally framed around Markov Decision processes (MDP). This can be thought of as a stochastic chain of events that is applied to a decision process known as a policy function [112]. When in a state, the agent must decide what the best action is and ensure it will achieve the desired state in RL terms of learning a Q-function. This is important because the algorithm will need to be either on- or off-policy; where for on-policy probabilities of better-discounted rewards are summed to pick the highest probability chain, or for off-policy where a mechanism is introduced to greedily make decisions for the best Q-function [112]. Where Q-function is a variant of a value function in RL which tries to directly determine the best possible action within a state, vs an action which one tries to find the optimal state then maximize the chances

of being in it. The next relevant item concerns the importance of a model in the RL program. The nature of classical dynamic programming methods often requires a model for acceptable use of an MDP [112]; this limits the generalizability of the method and model-free approaches are desirable. Lastly, in considering generalizable algorithms large-action space cardinality is critical in the efficient exploration of the optimal policy. From a high level, this is efficiently done with actor-critic methods and was an essential element in the selection of the method. Details on the dueling deep neural networks are past the scope of this work and the reader is referred to [112] for more information.

The work by [110] for a simple case considered an algorithm known as Double Dueling Q Networks (DQN) which considers only discrete actions. In terms of exploration of a high dimensionality space continuous variable exploration is ideal and the Deep Deterministic Policy Gradient (DDPG) algorithm was selected [113]. The algorithm is a model-free, off-policy, actor-critic-based algorithm. From a technical perspective, the actor-critic element allows for the exploration of continuous action space, and the policy estimation and update use a DQN algorithm [113]. The previously published algorithm that has been extensively used in the literature is presented in Figure 14, to explain its relevance in design optimization.

Figure 14

DDPG Algorithm As Presented in [113]

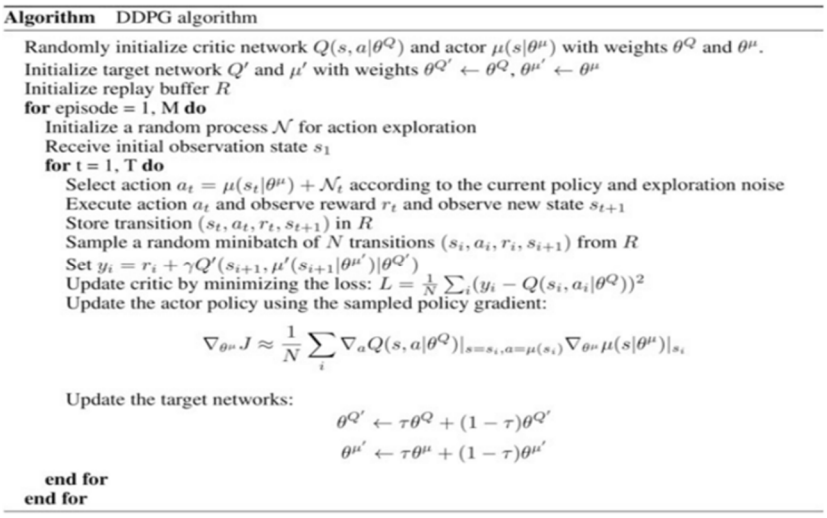

Algorithm DDPG algorithm

Randomly initialize critic network $Q(s, a|\theta^Q)$ and actor $\mu(s|\theta^\mu)$ with weights θ^Q and θ^μ.
Initialize target network Q' and μ' with weights $\theta^{Q'} \leftarrow \theta^Q$, $\theta^{\mu'} \leftarrow \theta^\mu$
Initialize replay buffer R
for episode = 1, M **do**
  Initialize a random process $\mathcal{N}$ for action exploration
  Receive initial observation state s_1
  for t = 1, T **do**
    Select action $a_t = \mu(s_t|\theta^\mu) + \mathcal{N}_t$ according to the current policy and exploration noise
    Execute action a_t and observe reward r_t and observe new state s_{t+1}
    Store transition (s_t, a_t, r_t, s_{t+1}) in R
    Sample a random minibatch of N transitions (s_i, a_i, r_i, s_{i+1}) from R
    Set $y_i = r_i + \gamma Q'(s_{i+1}, \mu'(s_{i+1}|\theta^{\mu'})|\theta^{Q'})$
    Update critic by minimizing the loss: $L = \frac{1}{N}\sum_i (y_i - Q(s_i, a_i|\theta^Q))^2$
    Update the actor policy using the sampled policy gradient:

$$\nabla_{\theta^\mu} J \approx \frac{1}{N} \sum_i \nabla_a Q(s, a|\theta^Q)|_{s=s_i, a=\mu(s_i)} \nabla_{\theta^\mu} \mu(s|\theta^\mu)|_{s_i}$$

    Update the target networks:

$$\theta^{Q'} \leftarrow \tau\theta^Q + (1-\tau)\theta^{Q'}$$
$$\theta^{\mu'} \leftarrow \tau\theta^\mu + (1-\tau)\theta^{\mu'}$$

  end for
end for

The algorithm in Figure 14, shows algorithmically that all desired criteria are present in the DDPG algorithm for general applications. In addition, the exploration noise (Ornstein-Uhlenbeck) is injected via random process to help preemptively address convergence to a local extremum, which makes the method applicable to solve non-linear programming problems such as optimization of continuum structures. The DDPG algorithm has been implemented on a plethora of repositories. Actions passed from the RL agent (DDPG policy) are representative of the dimensions of the cantilevers in the analytical model under the same constraints as the FA implementation. While Ornstein-Uhlenbeck noise should theoretically help ensure global convergence, the routine is run at least five times with random seeds used for each of the 500 episodes with a batch size of 16. Ornstein-Uhlenbeck noise is the same stochastic function type used in FA that allows to solve nonlinear optimization problems.

4.4.2. *Implementation*

The DDPG algorithm has been implemented on a plethora of repositories. For purpose of simplicity, the stable-baselines variant based on baselines by Open AI [114] was used in our implementation. The developed analytical model in the previous sections was selected as the environment for direct comparison with the modified FA approach from Section 4.3. In the RL paradigm used, each episode consists of a singular action similarly as in [111], and in each step, the reward function is updated. Furthermore, the reward function mimics the cost function presented in equation 30. Actions passed from the RL agent (DDPG policy) are representative of the dimensions of the cantilevers in the analytical model under the same constraints as the FA implementation. While OA-noise should theoretically help ensure global convergence, the routine is run at least five times with random seeds used for each of the 500 episodes with a batch size of 16. A schematic of the interactions between the RL agent and encompassing environment is shown in figure 15.

Figure 15

Schematic Outlining the Interactions Between the RL Agent and Environment

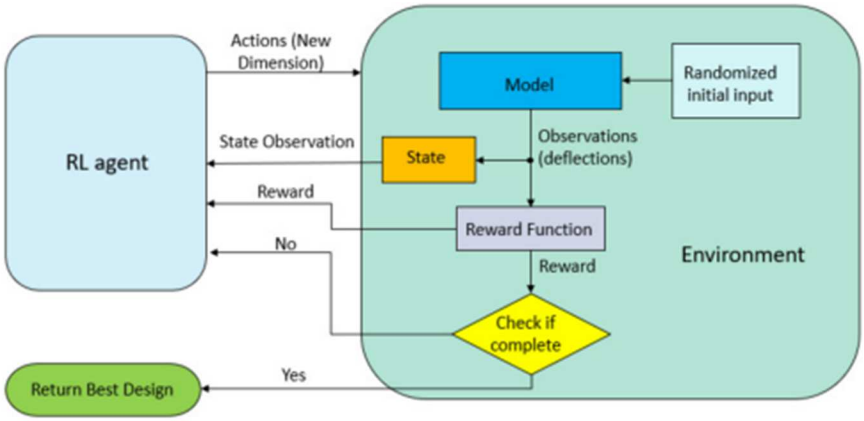

Note. This interaction between The RL agent and the environment for the employed RL-based optimization [30].

4.5. Comparison of Model-Based Simulation Results

Results of both FA and DDPG algorithms are compared for the model-based approach to assess their performance and discussion on the optimal air chamber topologies. The FA algorithm with memory is extremely fast to converge whereas the DDPG method is significantly slower. This is expected because DDPG will make the decisions based on a Q-function which is inherently probabilistic. Where Q-function is a variant of a value function in RL which tries to directly determine the best possible action within a state, vs an action in which one tries to find the optimal state then maximize the chances of being in it. However, over time both can converge to an optimum value. Cost- and Reward- step plots are presented from [30] along with the optimum designs in Figure 16.

Figure 16

MatLab and DDPG Plots and Results

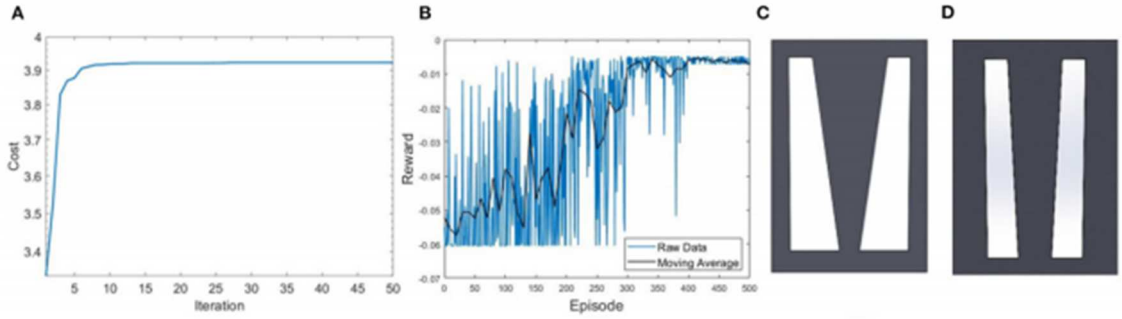

Note. Comparison of the (A) cost function values with respect to the number of-iterations in FA optimization, and (B) reward step plots from DDPG optimization for the model-based optimization routines, along with the resultant air chamber topologies. (C) FA resultant chamber topology. (D) DDPG resultant chamber topology.

Further examining the results from the model-based optimization, the FA-based optimization estimates 15 mm of horizontal motion about the leftmost cantilever; while the DDPG-based optimization estimates 10.3 mm. Assessment of the air chambers shows larger chambers and thin wall vertical beams in the FA-based design that may be prone to large deflections in the vertical direction due to the lack of a supporting structure. , Ratios of the beam's top and bottom dimensions were considered as a metric to describe beam layout [30] in both FA- and DDPG-based optimization, the outer beams were slender with the ratio $\frac{b_1}{L_1'} = 0.9$, while for the central cantilever ratio $\frac{b_2}{L_2'}$ was 3.6 for FA and 1.2 for DDPG-based optimization. The selection of a V-shaped central beam amongst both shows that it is more likely the optimal configuration than an A-shaped topology, which

intuitively makes sense and is in accordance with the design based on our engineering intuition [29]. Due to the limitations of the analytical model and the need for validation, an FE-based computational model and experimental analysis are presented in the following section for each design.

4.6. Extension to Direct Shape Optimization with FE-Based Model

To better realize full potential of the RL-based optimization method and extend it to higher dimensionality systems, an FE-based model was created and coupled with the RL agent via PYANSYS [115]; which serves as a Pythonic interface to Mechanical ANSYS Parametric Design Language (APDL). In our approach, we created four nodes confined to one-half of the actuator with free range to create a quasi-unconstrained environment [30]. The nodes comprise a closed and evolving quadrilateral that is mirrored through the line of symmetry of the actuator to create the second air chamber. Four points are selected to allow for a closer comparison between the FE-based model and the analytical-based model approaches. Each node can have 2 possible actions associated with a change in the x- and y- position, creating a total of 8 actions. Therefore, the control of the x-and y- coordinates directly corresponds to the actions from the RL agent, totaling up to eight. For the special case of horizontal motion, only four actions are used, each corresponding with motion in the x- direction for each node. The second component in the vertical direction is constrained in all for a direct comparison and results validation with the model-based formulation which only considers the horizontal displacement. Chamber configurations presented as line plots are shown in Figure 17 for the simulation with 8 actions.

Figure 17

Evolution of Node Configurations and Chamber Layout

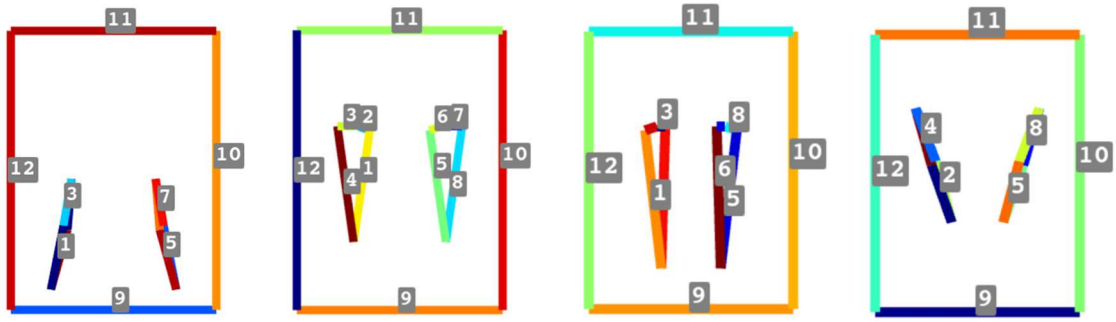

Note. Provided line plots show comprehensive exploration of the design space for "A-shaped" and "V-shaped" shaped chambers and beams. In order from left to right designs are at steps 26, 147, 197, and 216 of 500 total episodes. For cases where chambers are not close to the base, the tubing would have been run to the base of the chamber.

The FE-based RL program was run for each number of possible actions. In each case, the reward function mimics that of the analytical variant. The FE model utilizes a fixed boundary condition at the base and applies pressure to the chamber walls with the same magnitude as the analytical model for direct comparison. 8-node plane elements with a 7.5×10^{-4} m face sizing and the Hexa-dominant method are used for meshing. The FE elements (Plane-183) were selected for its capacity to handle large deflections and support hyperelasticity. With each step in the RL program, the location of the node corresponding to the middle of the central and rightmost cantilever will change, and therefore the closest node is returned in a multimodal fashion for a neighborhood of 1.2 mm in x- and y- directions. Results of the convergence and the optimized chamber and

beam geometry for 8-action and 4-action FE-based method are as presented in [29] are shown in Figure 18 (a-c) and (d-f), respectively.

The 8 DOF implementation considers 8 actions from the RL agent corresponding to a node location, positioned at a vertex of an air chamber modeled as a quadrilateral. In the cost function for the showcased results both horizontal and vertical motions are considered in the cost function.

Figure 18

Results from FE-Based RL Optimization

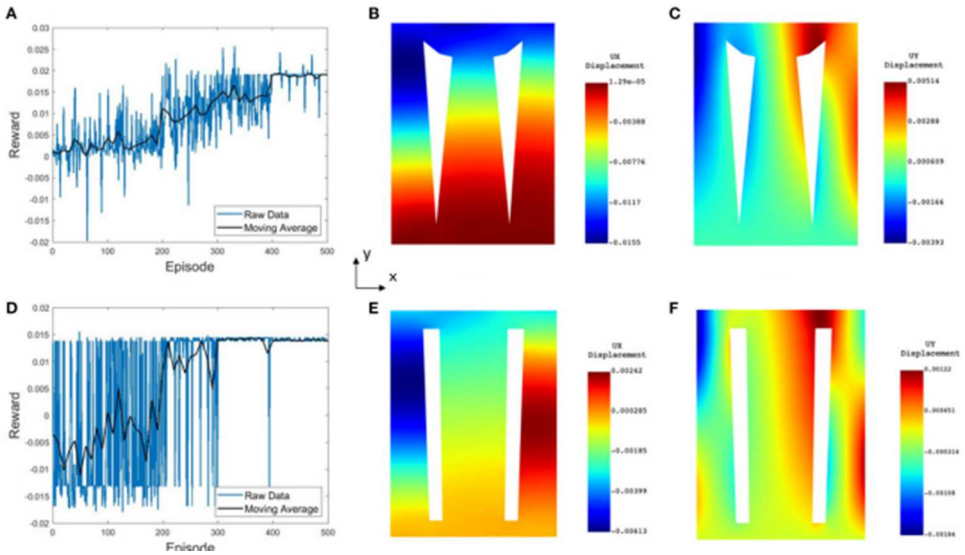

Note. FE-based environment with DRL optimization results where (A-C) are the results for the 8-action model with horizontal and vertical displacement considerations, and (D-F) presents the results for the 4-action model for only horizontal motion. (A, D) presents convergence for the 8- and 4- action models, respectively. (B, E) presents horizontal displacement contours where lowest values (dark blue bands) are considered for maximal displacement, and (C, F) show vertical displacement contours for the 8- and 4-action models, respectively.

Figure 18 shows stable convergence for the RL-based optimization with higher dimensionality offsetting the convergence rate. This could set reasonable computational limits for studies with the extremely large dimensionality. In the eight-action simulation, maximal deflection approaches 15.5 mm and for the four-action simulation, it approaches 6 mm. This implies that control over the vertical components of the cantilever vertices

may help and is a possible future direction for the analytical modeling. Furthermore, the relative order of the deflections, especially the eight action FE model, closely resembles that of the analytical-based model, showing merit in the methodology. Examining the vertical and horizontal contours qualitatively, the actuation principle closely resembles bending; which intuitively it works without reinforcements. It is observable, however that the topology will impact how extreme the bending is and that the distribution – particularly observing horizontal- is not directly linear from diagonal tip-to-tip of the actuator. In the next section, a computational model to validate all optimized actuators along with fabrication and experimental validation is presented.

Chapter 5

Finite Element Modeling and Experimental Validation

5.1. FE Computational Model for FA and DRL-Based Optimization

In order to reduce the cost and time needed to validate the results experimentally, the performance of the actuators was first determining by developing a finite element model results using ANSYS FE solver. Each actuator was designed in SolidWorks and validated using computational models.

The material models which were derived and explained in Chapter 3 were used to derive the material model coefficients. The material model coefficients were used as an input into the ANSYS Workbench. In order to support large strains and hyperelasticity our actuator was modeled using SOLID186 higher order 20-node and SOLID187 higher order 10-node elements.

Basic shape of elements, distortion of elements, polynomial order of elements, material incompressibility, and integration techniques are factors that affect the convergence of the finite element solutions characteristics significantly [116]. In order to achieve more accurate and efficient results in structural analysis, using quadrilateral and hexahedral meshes is preferred for two-dimensional and three-dimensional meshes, respectively. In general, quadrilateral elements are superior to triangular elements [117]. Due to the above-mentioned reasons, a uniform, medium smoothing, hex-dominant mesh was chosen. To check the effect and validate the convergence of the solutions, the size of FE elements was intentionally varied from 1.5 mm (108,235 nodes) to 2.1 mm (43,508 nodes). The results of the mesh size effect are presented later in this section.

The base of each actuator was fixed and pressure/vacuum with the amounts of +12/-5 psi was increased incrementally inside each chamber concurrently. In each step the amount of applied positive pressure inside the chamber was increased by 0.13044 psi and inside the chamber with the applied vacuum pressure was decreased by 0.05434 psi. Frictionless contacts were defined between two sides of each chamber in order to prevent the sides to penetrate each other when vacuum is inserted. Actuators were sliced in half revealing their inner geometry. The simulation was applied only on half of each actuator for simplification and decreased computational time purpose. Using symmetry region on the cross section of the sliced actuator, the desired results were provided for the whole actuator.

Material's stress-strain data were measured experimentally as explained in Chapter 3 and imported into ANSYS software. The best fitted hyper-elastic material model was determined and fitted curves and material coefficients were provided by ANSYS. Using this as an input to ANSYS material section, directional displacements/deformations, principal stresses, and principal strains were analyzed for each model.

After obtaining satisfactory results in ANSYS simulation, each actuator was fabricated from soft silicone rubber to be tested experimentally. Each actuator was tested and the displacements were measured using DIC method to obtain accurate displacement field results. The DIC method is explained in more details in next section.

5.2. Experimental Validation Using DIC

Digital Image Correlation (DIC) is an ideal technique used to measure and study material deformation and crack propagation in engineering applications [118]. This innovative technique is accurate, non-invasive and relatively simple. DIC has been defined as an optical, non-contact method for determining displacement and strain [119].

In order to utilize DIC method for strain measurements, sequential camera images are taken and each image is divided into interrogation cells or subsets which are groups of pixels. Smaller interrogation cells result in less precise strain rates [120]. However, it increases the data field's spatial resolution. This depicts the fact that accuracy of DIC measurement and spatial resolution relies on the resolution of the image. Size and density of the speckles within a pattern influence the precision of the measurement [120]. To facilitate DIC in our experiments, a random high-contrast speckle pattern was coated on the front surface of each actuator and each material characterization sample. The results obtained from the DIC were used to characterize the 3D strain components of each material sample and each actuator to perform both silicone rubber material characterization and to choose the best optimization method by comparing the corresponding results.

Figure 19

Digital Image Correlation Setup and Lighting

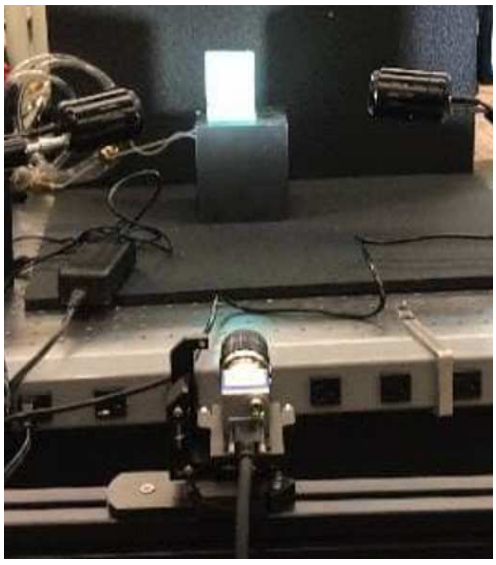

In this setup, a 3D printed box is placed under the actuator for preventing the tubes connected to the air chambers from being folded and to allow the tubes to supply pressurized air/vacuum to the air chambers.

In this work, a stochastic high-contrast speckle pattern is applied to a sample and is fed into a software which monitors changes in color in small areas of an image frame as a sample deforms to determine local displacements. A black speckle pattern was applied to each sample with spray paint. Samples were tested as the paint was drying due to the large strains displayed by the samples which would otherwise cause large paint chips. 3D DIC, which utilizes binocular stereo vision (two cameras that are synchronized) was used due to the possibility of out of plane motions from air chamber expansion and compression. This is observed in experimental data presented later. Prior to each test cameras were stereo calibrated with a 5mm calibration plate; this is done by taking a

series of images with a plate with markers of known distance between them. The software used (VIC 3D, Correlated Solutions) has an inbuilt system for calculations and a custom scoring system of proficiency in calibration. Across all the tests the averages of several camera conditions are considered. First, the rotation about the optical axis average is -0.84 degrees, second the stereo angle is -17.25 degrees, last the tilt is 0.96 degrees. Images were acquired at 0.5 fps simultaneously with each camera with vacuum first applied followed by positive pressure in the opposite chamber. For post processing a rectangular region of interest of the front face was used. Various step and sub step sizes were used largely due to the out of plane motion of some chambers requiring larger steps towards the end of tests. Both a fill boundary function to fill between edge spaces by interpolation and a low pass filter to remove high frequency information were used in running the correlation.

5.3. Experimental and Simulation Results of IntelliPad System

Simulation and experimental results of a single soft actuator under an applied external load on the top surface and the applied pressure and vacuum in the side chambers are shown in Figures 20 and 21 respectively. In both vertical and horizontal directions, the single actuator was undergoing free displacements. The air pressure and the vacuum in the top and side chambers were varied. The external load applied on the top surface also varied. The structural stability of the actuator was tested by not applying any pressure in the actuator chambers and applying an external load of 20 *kPa* [121]. The amount of the applied external load was determined based on to the average pressure at the cushion and human buttock interface to make simulate the case of air pressure system failure in the IntelliPad system the actuators are able to withstand the load and not

collapse. Test of applied *20 kPa* (2.9 *psi*) normal load resulted in a 2.5 *mm* of vertical displacement.

Figure 20

A Single Actuator's Characterization's Simulation Results

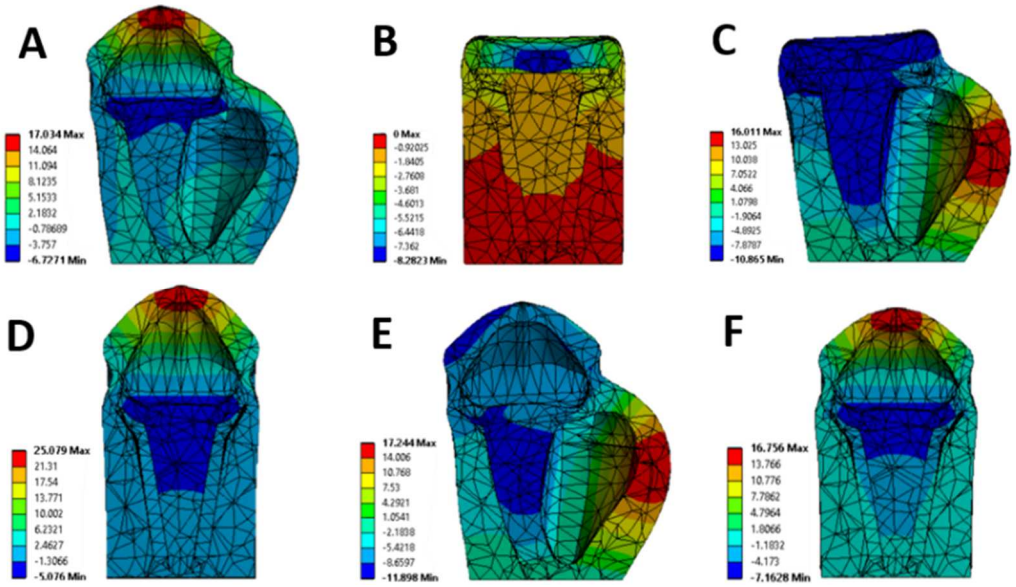

Note. A, free displacement in the horizontal direction for 10 *psi* positive air pressure in the right chamber, -5 *psi* negative air pressure in the left chamber, 15 *psi* in the upper chamber. B, displacement of the actuator in the vertical direction when no pressure is applied and only 2.9 *psi* [121] as the external load is applied to the top portion of the actuator in order to support the human weight. C, free displacement of the actuator in the horizontal direction by applying 10 *psi* positive air pressure to the right chamber and -5 *psi* in the left chamber. D, free displacement of the actuator in the vertical direction when applying 15 *psi* in the top chamber. E, the displacement resulted from applying 15 *psi* in the top chamber, 10 *psi* in the right chamber and -5 *psi* in the left chamber. F, free displacement of the actuator in the vertical direction when applying 15 *psi* in the top chamber and 2.9 *psi* as an external load on top of the actuator. All units are in millimeters.

Figure 21

A Single Actuator's Characterization's Experimental Results

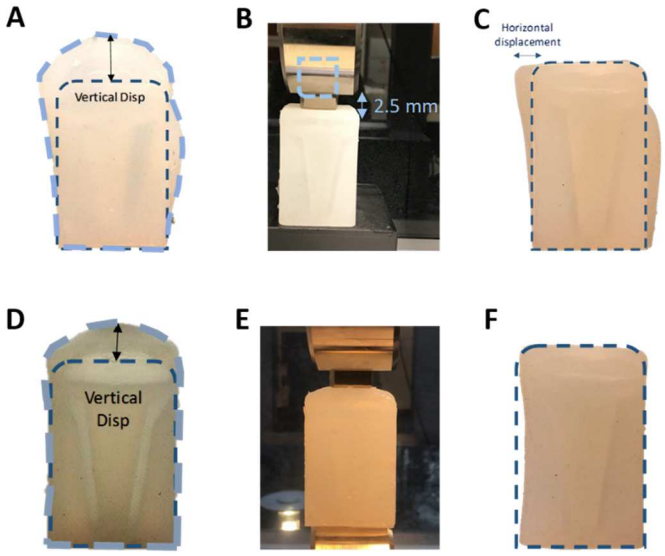

Note. A, free displacement in the horizontal direction for 10 *psi* positive air pressure in the right chamber, -5 *psi* negative air pressure in the left chamber, 10 *psi* in the upper chamber. B, displacement of the actuator in the vertical direction when no pressure is applied and only 2.9 *psi* [121] as the external load is applied to the top portion of the actuator in order to support the human weight. C, free displacement of the actuator in the horizontal direction by applying 10 *psi* positive air pressure to the right chamber and -5 *psi* in the left chamber. D, free displacement of the actuator in the vertical direction when applying 15 *psi* in the top chamber. E, free displacement of the actuator in the vertical direction when applying 15 *psi* in the top chamber and 2.9 *psi* as an external load on top of the actuator. F, horizontal displacement resulted from applying only vacuum in the left chamber.

The pressure in the top chamber was gradually increased from 0 to 20 *psi* and the corresponding displacement of the top surface of the actuator was measured using the tensile machine with no external load applied. Both experimental results and the simulation results showed similar amounts for the maximum applied air pressure of 20.9 *psi* with matched maximum vertical displacement of 31.5 *mm* see Figure 22.

Figure 22

Simulation and Experimental Results of Free Displacement in Vertical Direction

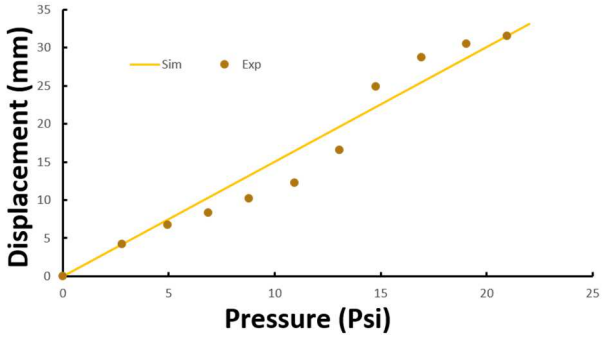

Note. Positive air pressure applied only in the top chamber of a single actuator.

The maximum amount of horizontal displacement resulted from the simulation was 10.8 mm and this displacement in the experimental set up showed 7 mm of displacement. This slight discrepancy could have happened due to warping of the bottom surface of the actuator which results in different boundary conditions or possibly due to the air pressure leakages in the side chambers.

5.3.1. *Shear Relaxation Experiments*

To test the actuators for their capability to prevent blister formation, three similar masses were placed on top of three actuators which were positioned 15 mm apart. A compression spring was integrated between each two masses and FSR sensors were placed between the springs and on top of each actuator. We fixed two masses and applied a horizontal load to the side mass which was free to move. This resulted in compressing the springs that were placed in between these two masses. The FSR sensors that were placed in between each two masses measured the amount of the applied load. This horizontal load resulted in a shear force being created on top of the actuators. By actuating the soft actuator in the middle by applying positive pressure in one chamber and vacuum in the other, we demonstrated the potential for mitigation of the created shear forces at the contact interface, see Figure 22. This happened due to the horizontal displacement of the top surface of the center actuator which resulted in relaxation of the springs in between two masses and reaching an equilibrium position. This equilibrium and reduced shear force was recorder using FSR sensors in between two masses which is shown in Figure 23 (a).

Figure 23

Shear Relaxation Experimental Setup

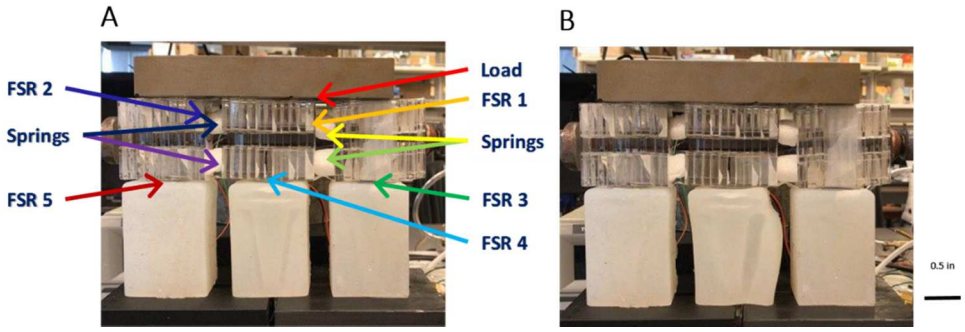

Note. A, prestressed initial shear condition. B, movement of the center actuator towards left, resulting in the shear relaxation condition.

Figure 24

Shear Force and Pressure Profiles Recorded Using FSR Sensors

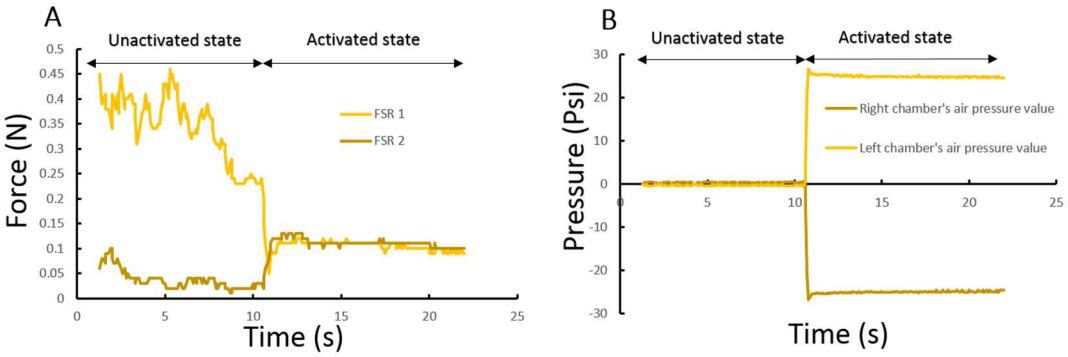

Note. A, pre-load and after air pressure application inside the chambers conditions for producing horizontal displacement to reach equilibrium for shear force, and B, pressure profiles recorded by the FSR sensors.

5.3.2. *Normal Load Distribution Experiments*

In order to test the capabilities of the actuators for regulating the external normal load, an experimental setup was considered using two actuators, see Figure 24. The algorithm measures both the external applied forces using FSR sensors integrated on top the actuators and also considers the amount of pressure applied in the top chambers. Considering this, based on the difference in the external load applied on each actuator and the average of the applied pressure, the algorithm either reduces the pressure in the top chamber of each actuator or increases the pressure. In the experiment while one of the actuators was not pressurized, an initial pressure of 18.4 psi was applied to the top chamber of the other actuator. We placed a 1.6 kg block of steel on top of the actuators.

Figure 25

Experimental Setup of Normal Load Distribution

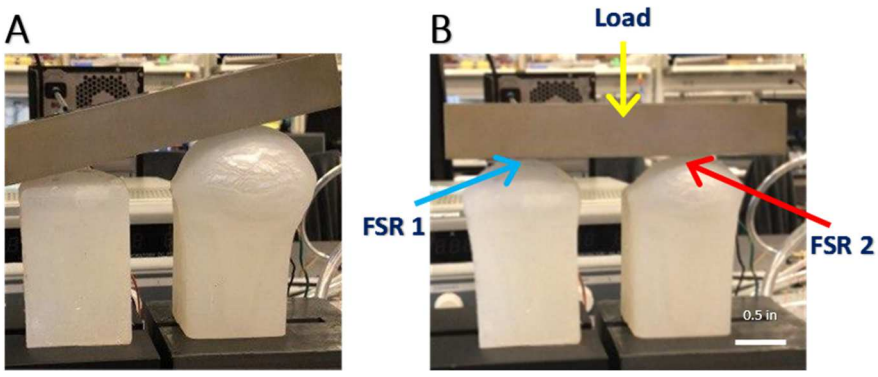

Note. This experiment aimed to test the algorithm and demonstration of the capabilities of the actuator for normal load distributions. A, unbalanced normal load condition. B, equilibrium state of the load distribution.

After calibrating each FSR the applied external load was recorded. Initially most of the weight of the metal block was supported by only one of the actuators. the differential existing in the reading of the external load by the controller sends a command to pressurize the unloaded actuator by activating the solenoids. By measuring the pressure, the amount of inflation can be controlled. Using this we can distribute the weight evenly across both actuators until the differential of the forces shows a net-zero result. Over the span of 0 to 0.45 sec the loading was applied, see Figure 25.

Figure 26

External Normal Load Distribution Control Using FSR Sensors

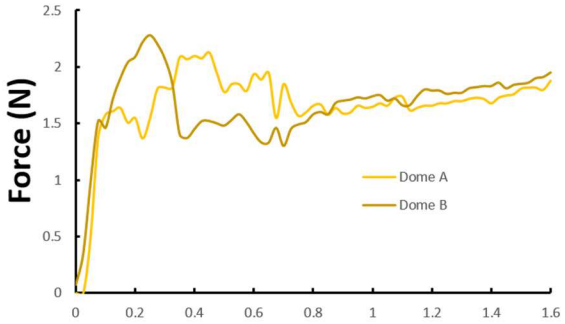

Note. This graph indicates the control of loading, active control, and equilibrium phases of the two actuators used in the normal load distribution experiment.

5.4. Experimental Results and FE-Based Computational Model

In the experiments, the base of each actuator was fixed to a platform mimicking the attachment used in the ANSYS simulation. A vacuum of -5 *psi* was applied to the left

chamber and a 12 *psi* positive air pressure to the right one. Using 3D DIC method the full-field response of each actuators displacement is characterized and recorded, see Figure 27. In order to pick and evaluate the best optimization method, free deformation of the top surface and the horizontal displacement of each actuator was evaluated and compared both experimentally and using FE computational software. Figure 27 illustrates the horizontal inner displacement of each actuator at the center cross-section. The largest horizontal displacements were obtained from the FA-based and empirical designs. A comparison between the experimental results and the FE computation models shows the same trends of displacement contour maps in both vertical and horizontal motions of each actuator.

As shown in Figure 27, the ranges of strain determined in this work from FEM and DIC allows us to assume nearly linear behavior for strains up to for optimization purposes of the material used in this study.

Figure 27

Experimental (DIC) and Simulation (ANSYS) Results

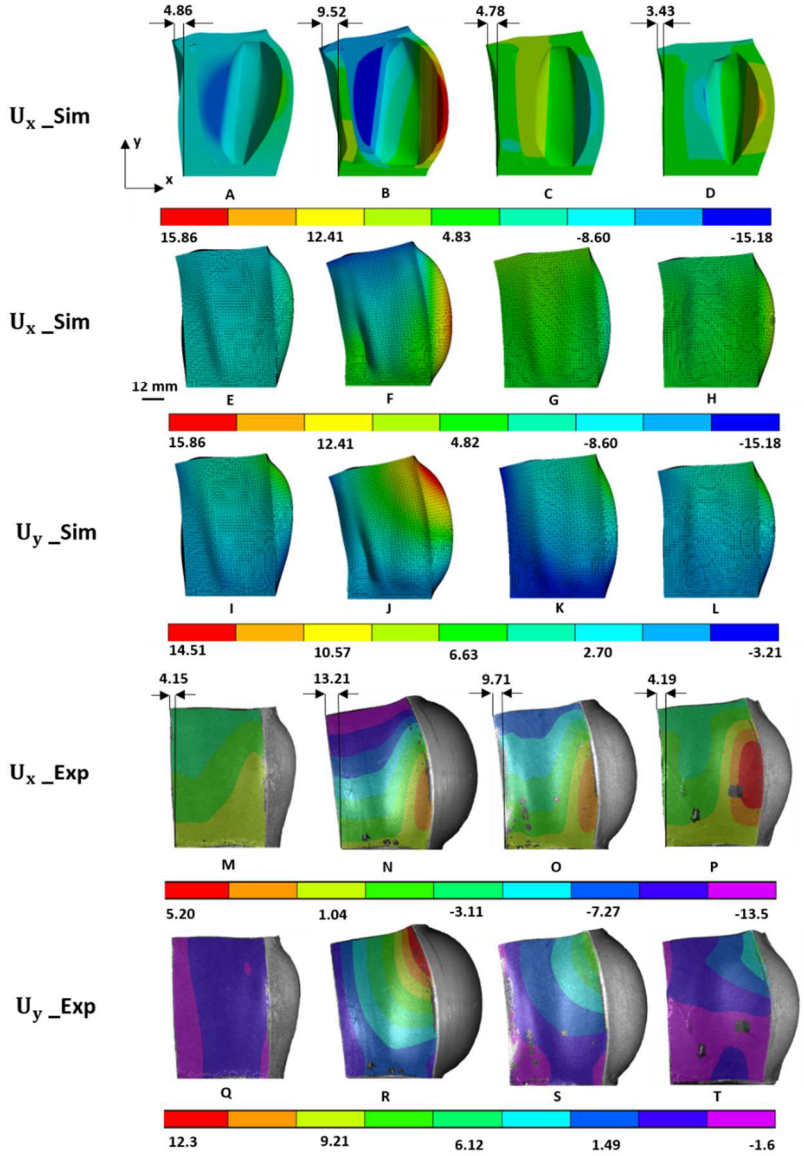

Note. DIC experimental (Exp) results and ANSYS simulation (Sim) results of horizontal and vertical motions of the original and optimized actuators in x, (U_x) and y, (U_y) directions in mm. (A,E,I,M,Q) Original Actuator, (B,F,J,N,R) Model-based FA, (C,G,K,O,S) Model-based DDPG, and (D,H,L,P,T) 8-DoF FE-based [30].

Using various methods of optimization in this work resulted in improvements of the optimized actuators functionality in the corresponding achieved horizontal motions. The optimized FA-model based design showed an increased amount of 4.66 mm compared to the original empirically designed actuator. The DDPG-based optimized design showed 0.09 mm less amount of deflection compared to the original one empirical design which was 4.78 mm. On the contrary, it showed a 1.01 mm improvement in minimizing the displacement in the vertical direction. This was not achieved by the FA model-based design.

Regarding our cost function, which considers the tip of the first cantilever to optimize the horizontal displacement, we only compare the displacements of each actuators tip. A comparison of the ratios of (Y_{01_y}/Y_{01_x}) for all designs is presented in the Figure 28, in which Y_{01_y} and Y_{01_x} stand for vertical and horizontal displacements respectively. These ratios are presented to show decoupling of degrees of freedom at the condition of steady pressure. In order to reach a better decoupling, a smaller ratio is desirable as it indicated better decoupling between x- and y- displacements. All the optimized designs resulted from FA and DDPG-based outperformed the original empirical design. All DDPG-based optimized designs depicted lower decoupling ratios than FA based on experiment results which, indicates a better performance. However, the optimization design resulted from FA provided the largest horizontal displacement.

Figure 28 shows the comparison of ratios between maximum horizontal and vertical displacements for all simulation and experimental results. The ratio of vertical to horizontal displacement in DDPG-based design was 0.39, which was almost half the ratio of the empirical design (0.20). Although the aimed motion for the actuators was to

capture pure planar motion all actuators displayed some bending motion as well. The reason for this is that 2-D model formulation was used instead of a 3-D model formulation and the hyperelastic behavior of the material used in this study and other assumptions made in the analytical modeling for the purpose of simplifying the process. As shown in Figure 28, the 8 DOF FE-based design has the lowest displacement ratio, which was the reason for fabricating and experimentally validating this design rather than 4-DOF design.

Figure 28

Comparison of Decoupling Ratios of Each Design's Maximum Horizontal and Vertical Displacements.

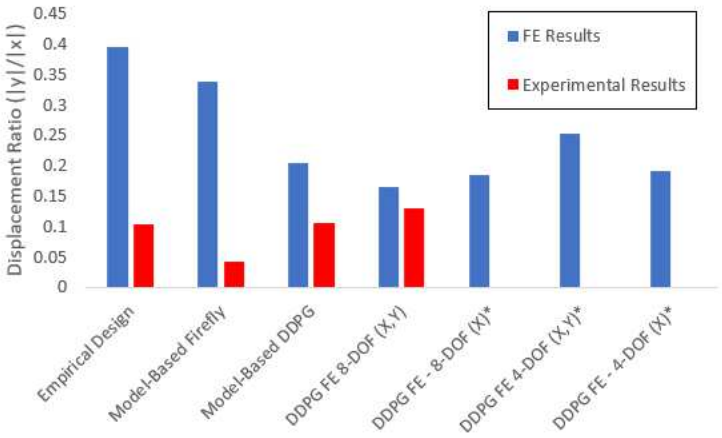

Note. For the optimization section various cost functions were considered. Other designs that were designed and evaluated using FE but were not chosen to be manufactured and tested experimentally are designated with *.

Figure 30 shows the relationship of the horizontal and vertical displacements as a function of applied pressure. The positive air pressure and vacuum were simultaneously

applied with same rates, both achieving their respective maximum values at 12 psi and -5 psi, respectively. This relationship also depends on the applied pressure/vacuum in the air chambers. As explained in Section 5.1, various element sizes from 1.5 mm to 2.1 mm were used for meshing the designs in FE computational models. Figure 30 (B) shows the convergence for various number of nodes used in FE computation model performed for only model-based FA design. Element sizes of 1.5 mm were chosen for all other performed simulations, due to relative small actuator size and reasonable computational time, despite showing that the mesh size did not have a significant effect on the displacement results. In both DDPG and FA optimization methods we assumed a linear behavior for our material in the applied pressure range. On the contrary in our ANSYS models we imported the experimental data derived from tensile test which was non-linear. Since the behavior of the relationship between horizontal displacement and the applied pressure is almost linear, it validates the proposed optimization methods for this pressure range. The performance of the DDPG-based optimized designs in Figure 30 is the best example for this. However, Figure 30 show a non-linear relationship between the vertical displacements and applied pressure.

Figure 29

Relationship Between Applied Pressure and the Corresponding Horizontal Displacements

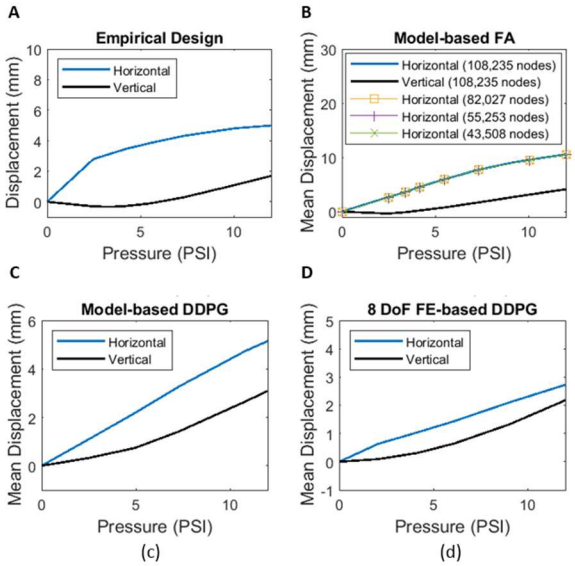

Note. FE-based computational models are used to obtain the relationship for all **(A)**. Empirical design, **(B)** model-based FA and the convergence for nodes in model-based FA, **(C)** model-based DDPG, **(D)** 8-DoF FE based DDPG optimization designs.

To improve the decoupling ratios of the actuators, vertical dynamics of the actuators must be considered deeper and the analytical models must be improved further. To achieve this, cantilever beams must be replaced with constrained beams in the analytical model. All FE based designs show similar results for displacement ratios. This is an implication of dependency of the cost function on the horizontal motion for effective use.

As it is clear while observing the designs, thinner side walls and larger chamber sizes would lead to greater deflection and horizontal motion. This results in lowering the

mechanical stiffness of the actuator in the vertical direction that lowers the amount of load bearing of the actuator, which is as important as maximizing the horizontal motion. The weight bearing is an important factor to consider when the soft actuator needs to tolerate the weight of a person in decubitus ulcer and blister injury prevention systems. The resulted lowered stiffness creates larger amounts of bending motion which was undesirable effect in the optimization process as part of this work. All the above-mentioned objectives exemplify the need for creating an optimization scheme for maximizing the horizontal motion while minimizing the vertical displacement.

Optimization routines were separately run ten times to evaluate their computational performance. DDPG takes 3.28 times as long as the firefly based validation method. In addition, the firefly method is able to converge to its optimal solution in fewer iterations than the DDPG method. Furthermore, the DDPG based method ran multiple times, this is because it was documented that starting conditions could change the end result, if the routine gets stuck at an extremum, this however is not common because the method contains both a deterministic and stochastic part similarly like the firefly method which is well documented and suited for handling multimodal non-convex optimization problems. Despite the lesser computational performance, DDPG outperformed the FA-based optimization method as confirmed by the results from the ANSYS simulations. The aforementioned results only consider the model-based optimization. Finite element based environments were only considered for DDPG, and therefore a one-to-one comparison cannot be made there. A series of 500 episodes takes approximately 2.5 hours with DDPG-FE optimization; it is noted that ADPL must be

opened and closed between each episode to consider the design changes, which significantly adds to the computation time.

Figure 30

Comparison of FA vs. DDPG-based Run Times for Model-based Optimizations

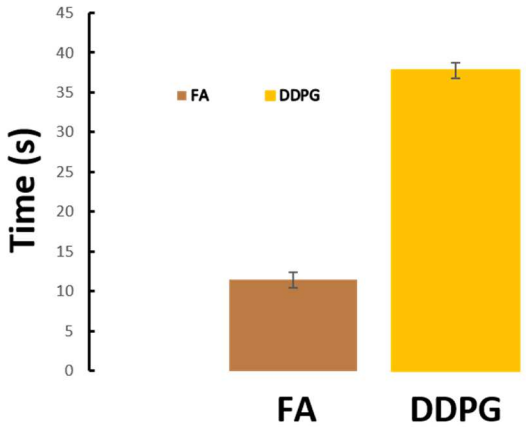

Note. Optimization routines were separately running ten times to evaluate their computational performance.

In addition, the firefly method is able to converge to its optimal solution in fewer iterations than the DDPG method. Furthermore, the DDPG based method is run multiple times, this is because it was documented that starting conditions could change the end result, if the routine gets stuck at extrema, this however is not to common because the method contains both a deterministic and stochastic part like the firefly method which is well documented and suited for handling multimodal non-convex optimization problems. Despite the lesser computational performance DDPG outperformed the FA base validation method, and is shown to be the better method from the ANSYS simulations.

The aforementioned results only consider the model-based optimization. Finite element based environments were only considered for DDPG, and therefore a one-to-one comparison cannot be made there. A series of 500 episodes takes approximately 2.5 hours with DDPG-FE optimization; it is noted that ADPL must be opened and closed between each considered design; which significantly adds to the computation time.

In this study, results of the designs obtained from DDPG method outperformed the FA model-based design. This was the main reason for choosing DDPG over FA to implement it with a FE computational model. We validated the DDPG method to document its efficacy for handling global optimization problems that can avoid problem of finding the local minima or maxima as commonly observe by using the gradient methods caused by non-convexity of the solution space. In order to address some of these issues plenty of open-source DRL codes are able to provide suitable objective formulations for design optimization explorations. Consideration of this and a combination of FA-based optimization with FE model are directions acknowledged for our future work which are explained further in Chapter 7.

Chapter 6

Business Plan for Commercialization of the IntelliPad System

In this section, a business plan was provided in which the proposed product offers a practical solution to one of the open problems in pressure injury prevention. The proposed system has the capabilities to remedy cases associated with shear stresses that are not addressed by the existing commercial products or in the existing literature. In addition, its modular nature offers unique solutions to clients at all purchasing levels. Existing market solutions generally offer some form of customization due to the dynamic needs of clients [122], however, the proposed product is adaptable beyond the capabilities of the existing systems. Based on the evaluation done during this study, the expenses that pressure injuries pose to public health indicate that such a system with the proposed business plan have the potential for long term sustainment with a variety of clients. The cost and existing devices unfortunately offer moderate barriers to entry, and hurdles that would need to be overcome. The next steps for business planning include filing for patent protection, applying for grants to allow for continued research and development, and continued cost and profit modeling of the startup. In the next, and final chapter future extensions, and overall conclusions of this work are presented. The overall expenses for production of the system were evaluated in this section. The overall business plan included 5 figures and 2 tables. The original chapter was reviewed and approved by the thesis committee members, however, it is not being publicly available, due to the possible opportunities for potential future commercialization of the technology.

Chapter 7

Conclusions and Future Work

7.1. Summary of Actuator Design and Development

In this thesis, a novel multi-degree of freedom actuator was presented. The actuator shaped actuator consists of three air chambers and achieves actuation based on an applied pressurized air/vacuum input. Actuators were first iteratively designed empirically using CAD software and finite element analysis. They were then experimentally tested to demonstrate their mechanical performance and the ability to regulate contact pressure at the top surface by moving a mass in both the vertical and horizontal directions, while simultaneously being able to withstand predefined normal pressure loading conditions at the top surface. Later, a comprehensive optimization process was undertaken that considered the optimization of maximal horizontal motion of the actuator. In the formulation, the actuator was modeled as a system of three tapered and thickened cantilever beams connected in a structure by virtual spring elements. Euler-Bernoulli beam theory was used for calculation of beam displacements. While some of the assumptions are not valid for large strains that hyperelastic materials can display, the model is presented as an acceptable alternative to more cumbersome approaches such as the Timoshenko or Cosserat approaches.

The derived analytical model was used with both a modified firefly algorithm (FA), and a novel optimization method that used a deep reinforcement learning based approach employing the Deep Deterministic Policy Gradient (DDPG) method. The optimization cost and reward functions were defined to maximize the horizontal motion, while also decoupling the vertical motions. The methods are more suitable over linear

programming methods due to non-convexities present in the derived analytical model, that are further visualized when plotting the solution space manifold of the cost function with respect to the optimized cantilever parameters. Both FA and DDPG methods display similar outer cantilever beam dimensions, with small variations in the slopes of the tapered beams. The DDPG-based optimization method was extended to use a FE-based environment, which ultimately yielded the best results in decoupling of degrees of freedom with added vertical deflection considerations that the analytical model in its current form is unable to capture.

Materials are characterized in quasi-static conditions, and in-situ DIC is used for characterization of the Poisson's ratio. Over the span of the work, two materials are considered, however, Elite Double 22 silicone rubber is selected as the final material for fabrication of future actuators. Experimental data is used to describe the non-linear hyperelastic behavior and modeled with the Ogden model used in the simulations that serve to validate optimization results prior to fabrication. The empirically designed, model-based firefly and DDPG, and 8-DOF FE-based DDPG actuators are fabricated using a multi-step molding approach.

The four selected actuators are modeled in ANSYS, and the deflections of physical actuators are characterized using DIC. Contour bands and relative magnitude of displacement in both the vertical and horizontal directions are consistent for all models. The firefly-based design shows the largest horizontal motions, but at the cost of large vertical motions that the analytical model cannot not capture. DDPG-based designs outperform both the empirical design and the firefly-based optimized design in FE simulation results, with the FE-based environment with DDPG showing the most vertical

to horizontal motion decoupling. In experimental results, the firefly design shows the largest decoupling capabilities, however, this was attributed to the experimental imperfection due to detached base of the actuator from the mounting surface. The empirical design and FE-based designs are of similar displacement magnitudes, with model-based DDPG performing the best in experiments. From computational modeling the FE-based DDPG design is selected as the optimal design for any future works due to having the most isolated horizontal motion.

A business plan is proposed for the integration of the designed actuator into a modular soft robotic pad named IntelliPad. The end use is aimed for controlled motion of the actuators surface to help with the prevention of pressure injuries. The proposed system will be specifically aimed at wheelchair users, and later for the bed-bound patients. The IntelliPad system will integrate force sensitive resistors to monitor normal and shear pressures, and redistribute load based on a feedback control system. To date, an active system that addresses shear in decubitus ulcers has not been proposed in industry or literature. A comprehensive search was conducted to validate this in patents, NSF grants, and literature.

The market analysis reveals the staggering costs associated with Hospital Acquired Pressure Ulcers (HAPUs) and identifies the likely end users of the product from clinical data. This is used to reinforce the benefits that Intellipad can offer for prevention and hospitalization cost minimization. Following the aforementioned multi-front competitive analysis, customers and market segments are identified and discussed in detail. It is revealed that this is a growing market, with customer interactions with all levels of the supply chain. When looking into the customer needs it is quantified that the

IntelliPad system covers a large portion of injuries end users experience from HAPUs. A preliminary cost analysis shows that the proposed system while relatively costly due to being the initial, full-scale prototype and considering the fact that the prototype will undoubtedly be costlier than production units from competitors, is still lower than the lowest estimates of related hospitalization costs and is thus a viable solution. Lastly, a SWOT analysis shows that the strengths and opportunities outweigh the weaknesses and threats in the realization of an IntelliPad system. In the next section proposed future works are presented.

7.2. Future Works

There are several avenues of work that can be explored with both the design of the individual soft actuator, and of the full IntelliPad system. In the analytical modeling of the actuator, a next step would be to consider vertical motions induced by the applied pressure/vacuum. This is one of the known limitations of the model, as shown in the computational model results. In addition, augmentation of the model to consider hyperelastic material properties by incorporating material models like Neo-Hookean, Ogden or similar, would help improve the accuracy of the results.

The physical actuators were manufactured with a multi-level casting technique. While this is efficient for one actuator, additive manufacturing could prove to be more robust for fabrication of many. There is also a need to improve the support at the base of the actuator, examining the experimental results from the firefly design, bowing can be seen at the base of the actuator. An active effort was made to remedy this during the work, but effective solutions are still needed. Lastly, clean sensor integration is still

needed for successful clinical use. The proposed sensor in NSF 0856387 is ideal for this application, and comparable techniques are under active consideration [123].

In experiments from [29], bowing about the base of the actuator was documented, and was a possible cause of discrepancy in the horizontal and vertical deflection between the experimental and simulation results. An effort was made to remedy this problem, by introducing a mesh to go at the base of the dome. The concept would have each dome of the IntelliPad system laying in a bed of the material used to fabricate the actuator, and hopefully minimize local bowing in the vertical direction. The design consisted of two parts for the individual dome. The main bed has holes in it to allow airflow to the dome, and is also a rest for the mesh which has extrusions to support the dome. For the experiments some improvement was noted, however, domes had a tendency to detach from where the material rested, and in future design iterations would require a deeper bed of material. In this work span, this was not explored due to limited material for fabrication. For large pressures small tearing was also present lending to the need to design an improved grid past the proof of concept presented.

There are several clinical considerations that lend to controls that should be addressed moving forward. A full system build is obviously the most direct extension of this work. To date, actuator prototypes have only been fabricated as validation of vertical and horizontal motions, and pressure redistribution [29, 30]. This device will need to be tested with tissue samples, or in a clinical population to validate its efficacy compared to the existing solutions. There is evidence regarding the effectiveness of vibration preventing pressure injury formation and increasing the blood flow in the corresponding regions [124]. We have considered using this advantage by integrating a vibratory system

into our future actuator design and control system. The current control system only considers redistribution of position to achieve a mean pressure in each plane. Deep learning is a promising candidate for understanding and addressing mapping problems in a variety of disciplines. NSF grant 177695 proposed this, and is a possible avenue of exploration if ample data is made available [125]. Overall, using information from the IntelliPad system to better understand and address the development of pressure injuries, is vital for both patients and the success of the device.

References

[1] D. Trivedi, C. D. Rahn, W. M. Kier, and I. D. Walker, "Soft robotics: Biological inspiration, state of the art, and future research," *Applied bionics and biomechanics,* vol. 5, no. 3, pp. 99-117, 2008.

[2] R. Pfeifer, F. Iida, and J. Bongard, "New robotics: Design principles for intelligent systems," *Artificial life,* vol. 11, no. 1-2, pp. 99-120, 2005.

[3] D. Rus and M. T. Tolley, "Design, fabrication and control of soft robots," *Nature,* vol. 521, no. 7553, pp. 467-475, 2015.

[4] B. Gorissen, D. Reynaerts, S. Konishi, K. Yoshida, J. W. Kim, and M. De Volder, "Elastic inflatable actuators for soft robotic applications," *Advanced Materials,* vol. 29, no. 43, p. 1604977, 2017.

[5] C. Majidi, "Soft robotics: a perspective—current trends and prospects for the future," *Soft robotics,* vol. 1, no. 1, pp. 5-11, 2014.

[6] L. Hines, K. Petersen, G. Z. Lum, and M. Sitti, "Soft actuators for small-scale robotics," *Advanced materials,* vol. 29, no. 13, p. 1603483, 2017.

[7] J. Rossiter and H. Hauser, "Soft robotics—the next industrial revolution," *IEEE Robot. Autom. Mag,* vol. 23, no. 3, pp. 17-20, 2016.

[8] C. Laschi and M. Cianchetti, "Soft robotics: new perspectives for robot bodyware and control," *Frontiers in bioengineering and biotechnology,* vol. 2, p. 3, 2014.

[9] S. Kim, C. Laschi, and B. Trimmer, "Soft robotics: a bioinspired evolution in robotics," *Trends in biotechnology,* vol. 31, no. 5, pp. 287-294, 2013.

[10] A. Albu-Schaffer *et al.*, "Soft robotics," *IEEE Robotics & Automation Magazine,* vol. 15, no. 3, pp. 20-30, 2008.

[11] M. Manti, T. Hassan, G. Passetti, N. D'Elia, C. Laschi, and M. Cianchetti, "A bioinspired soft robotic gripper for adaptable and effective grasping," *Soft Robotics,* vol. 2, no. 3, pp. 107-116, 2015.

[12] K. Chin, T. Hellebrekers, and C. Majidi, "Machine learning for soft robotic sensing and control," *Advanced Intelligent Systems,* vol. 2, no. 6, p. 1900171, 2020.

[13] J. C. Yeo, H. K. Yap, W. Xi, Z. Wang, C. H. Yeow, and C. T. Lim, "Flexible and stretchable strain sensing actuator for wearable soft robotic applications," *Advanced Materials Technologies,* vol. 1, no. 3, p. 1600018, 2016.

[14] M. Luo, M. Agheli, and C. D. Onal, "Theoretical modeling and experimental analysis of a pressure-operated soft robotic snake," *Soft Robotics,* vol. 1, no. 2, pp. 136-146, 2014.

[15] C. Laschi, B. Mazzolai, and M. Cianchetti, "Soft robotics: Technologies and systems pushing the boundaries of robot abilities," *Science Robotics,* vol. 1, no. 1, 2016.

[16] C. Laschi, "Soft robotics research, challenges, and innovation potential, through showcases," in *Soft robotics*: Springer, 2015, pp. 255-264.

[17] K. C. Galloway *et al.*, "Soft robotic grippers for biological sampling on deep reefs," *Soft robotics,* vol. 3, no. 1, pp. 23-33, 2016.

[18] C. Walsh, "Recent results from evaluation of soft wearable robots in clinical populations," in *International Symposium on Wearable Robotics*, 2018: Springer, pp. 58-62.

[19] J. Frame, N. Lopez, O. Curet, and E. D. Engeberg, "Thrust force characterization of free-swimming soft robotic jellyfish," *Bioinspiration & biomimetics,* vol. 13, no. 6, p. 064001, 2018.

[20] N. Takahashi, H. Takahashi, and H. Koike, "A Novel Soft Exoskeleton Glove for Motor Skill Acquisition Similar to Anatomical Structure of Forearm Muscles," in *2019 IEEE Conference on Virtual Reality and 3D User Interfaces (VR)*, 2019: IEEE, pp. 1568-1569.

[21] W. Dou, G. Zhong, J. Cao, Z. Shi, B. Peng, and L. Jiang, "Soft Robotic Manipulators: Designs, Actuation, Stiffness Tuning, and Sensing," *Advanced Materials Technologies,* p. 2100018, 2021.

[22] P. Polygerinos *et al.*, "Modeling of soft fiber-reinforced bending actuators," *IEEE Transactions on Robotics,* vol. 31, no. 3, pp. 778-789, 2015.

[23] A. Garriga-Casanovas, I. Collison, and F. Rodriguez y Baena, "Toward a common framework for the design of soft robotic manipulators with fluidic actuation," *Soft robotics,* vol. 5, no. 5, pp. 622-649, 2018.

[24] X. Chen, Y. Guo, D. Duanmu, J. Zhou, W. Zhang, and Z. Wang, "Design and modeling of an extensible soft robotic arm," *IEEE Robotics and Automation Letters,* vol. 4, no. 4, pp. 4208-4215, 2019.

[25] C.-P. Chou and B. Hannaford, "Measurement and modeling of McKibben pneumatic artificial muscles," *IEEE Transactions on robotics and automation,* vol. 12, no. 1, pp. 90-102, 1996.

[26] F. Daerden and D. Lefeber, "Pneumatic artificial muscles: actuators for robotics and automation," *European journal of mechanical and environmental engineering,* vol. 47, no. 1, pp. 11-21, 2002.

[27] S. Iamsaard *et al.*, "Conversion of light into macroscopic helical motion," *Nature chemistry,* vol. 6, no. 3, pp. 229-235, 2014.

[28] Y. Sun, J. Guo, T. M. Miller-Jackson, X. Liang, M. H. Ang, and R. C. H. Yeow, "Design and fabrication of a shape-morphing soft pneumatic actuator: Soft robotic pad," in *2017 IEEE/RSJ International Conference on Intelligent Robots and Systems (IROS)*, 2017: IEEE, pp. 6214-6220.

[29] M. Raeisinezhad, N. Pagliocca, B. Koohbor, and M. Trkov, "IntelliPad: Intelligent Soft Robotic Pad for Pressure Injury Prevention," in *2020 IEEE/ASME International Conference on Advanced Intelligent Mechatronics (AIM)*, 2020: IEEE, pp. 685-690.

[30] M. Raeisinezhad, N. G. Pagliocca, B. Koohbor, and M. Trkov, "Design Optimization of a Pneumatic Soft Robotic Actuator Using Model-based Optimization and Deep Reinforcement Learning," *Frontiers in Robotics and AI,* vol. 8, p. 107, 2021.

[31] P. Polygerinos *et al.*, "Soft robotics: Review of fluid-driven intrinsically soft devices; manufacturing, sensing, control, and applications in human-robot interaction," *Advanced Engineering Materials,* vol. 19, no. 12, p. 1700016, 2017.

[32] Z. Wang, P. Polygerinos, J. T. Overvelde, K. C. Galloway, K. Bertoldi, and C. J. Walsh, "Interaction forces of soft fiber reinforced bending actuators," *IEEE/ASME Transactions on Mechatronics,* vol. 22, no. 2, pp. 717-727, 2016.

[33] K. Suzumori, S. Iikura, and H. Tanaka, "Development of flexible microactuator and its applications to robotic mechanisms," in *Proceedings. 1991 IEEE International Conference on Robotics and Automation*, 1991: IEEE Computer Society, pp. 1622, 1623, 1624, 1625, 1626, 1627-1622, 1623, 1624, 1625, 1626, 1627.

[34] W. McMahan *et al.*, "Field trials and testing of the OctArm continuum manipulator," in *Proceedings 2006 IEEE International Conference on Robotics and Automation, 2006. ICRA 2006.*, 2006: IEEE, pp. 2336-2341.

[35] R. F. Shepherd *et al.*, "Multigait soft robot," *Proceedings of the national academy of sciences,* vol. 108, no. 51, pp. 20400-20403, 2011.

[36] B. Mosadegh *et al.*, "Pneumatic networks for soft robotics that actuate rapidly," *Advanced functional materials,* vol. 24, no. 15, pp. 2163-2170, 2014.

[37] B. C.-M. Chang, J. Berring, M. Venkataram, C. Menon, and M. Parameswaran, "Bending fluidic actuator for smart structures," *Smart materials and structures,* vol. 20, no. 3, p. 035012, 2011.

[38] P. Moseley, J. M. Florez, H. A. Sonar, G. Agarwal, W. Curtin, and J. Paik, "Modeling, design, and development of soft pneumatic actuators with finite element method," *Advanced engineering materials,* vol. 18, no. 6, pp. 978-988, 2016.

[39] M. De Volder and D. Reynaerts, "Pneumatic and hydraulic microactuators: a review," *Journal of Micromechanics and microengineering,* vol. 20, no. 4, p. 043001, 2010.

[40] B. Gorissen, C. Van Hoof, D. Reynaerts, and M. De Volder, "SU8 etch mask for patterning PDMS and its application to flexible fluidic microactuators," *Microsystems & nanoengineering,* vol. 2, no. 1, pp. 1-5, 2016.

[41] B. Gorissen, M. De Volder, A. De Greef, and D. Reynaerts, "Theoretical and experimental analysis of pneumatic balloon microactuators," *Sensors and Actuators A: Physical,* vol. 168, no. 1, pp. 58-65, 2011.

[42] K. Morimoto, A. Utsumi, and S. Konishi, "A design of longitudinally-divided balloon structure in PDMS pneumatic balloon actuator based on FEM simulations," in *2011 16th International Solid-State Sensors, Actuators and Microsystems Conference*, 2011: IEEE, pp. 2774-2777.

[43] A. D. Marchese, R. K. Katzschmann, and D. Rus, "A recipe for soft fluidic elastomer robots," *Soft robotics,* vol. 2, no. 1, pp. 7-25, 2015.

[44] O. C. Jeong and S. Konishi, "All PDMS pneumatic microfinger with bidirectional motion and its application," *Journal of microelectromechanical systems,* vol. 15, no. 4, pp. 896-903, 2006.

[45] Y. Shapiro, A. Wolf, and K. Gabor, "Bi-bellows: Pneumatic bending actuator," *Sensors and Actuators A: Physical,* vol. 167, no. 2, pp. 484-494, 2011.

[46] B. Gorissen, W. Vincentie, F. Al-Bender, D. Reynaerts, and M. De Volder, "Modeling and bonding-free fabrication of flexible fluidic microactuators with a bending motion," *Journal of Micromechanics and Microengineering,* vol. 23, no. 4, p. 045012, 2013.

[47] P. Shi, J. McPhee, and G. Heppler, "A deformation field for Euler–Bernoulli beams with applications to flexible multibody dynamics," *Multibody System Dynamics,* vol. 5, no. 1, pp. 79-104, 2001.

[48] J. A. Sol, A. R. Peeketi, N. Vyas, A. P. Schenning, R. K. Annabattula, and M. G. Debije, "Butterfly proboscis-inspired tight rolling tapered soft actuators," *Chemical communications,* vol. 55, no. 12, pp. 1726-1729, 2019.

[49] J. Till, V. Aloi, and C. Rucker, "Real-time dynamics of soft and continuum robots based on Cosserat rod models," *The International Journal of Robotics Research,* vol. 38, no. 6, pp. 723-746, 2019.

[50] R. W. Ogden, "Large deformation isotropic elasticity–on the correlation of theory and experiment for incompressible rubberlike solids," *Proceedings of the Royal Society of London. A. Mathematical and Physical Sciences,* vol. 326, no. 1567, pp. 565-584, 1972.

[51] M. Mooney, "A theory of large elastic deformation," *Journal of applied physics,* vol. 11, no. 9, pp. 582-592, 1940.

[52] P. Kohnke, "Ansys," in *Finite Element Systems*: Springer, 1982, pp. 19-25.

[53] M. H. Rosle, R. Kojima, K. Or, Z. Wang, and S. Hirai, "Soft Tactile Fingertip to Estimate Orientation and the Contact State of Thin Rectangular Objects," *IEEE Robotics and Automation Letters,* vol. 5, no. 1, pp. 159-166, 2019.

[54] N. Kato *et al.*, "Elastic pectoral fin actuators for biomimetic underwater vehicles," in *Bio-mechanisms of Swimming and Flying*: Springer, 2008, pp. 271-282.

[55] K. Suzumori, S. Endo, T. Kanda, N. Kato, and H. Suzuki, "A bending pneumatic rubber actuator realizing soft-bodied manta swimming robot," in *Proceedings 2007 IEEE International Conference on Robotics and Automation*, 2007: IEEE, pp. 4975-4980.

[56] Y. Matia and A. D. Gat, "Dynamics of elastic beams with embedded fluid-filled parallel-channel networks," *Soft robotics,* vol. 2, no. 1, pp. 42-47, 2015.

[57] A. A. Sipos and P. L. Várkonyi, "The longest soft robotic arm," *International Journal of Non-Linear Mechanics,* vol. 119, p. 103354, 2020.

[58] F. Boyer, V. Lebastard, F. Candelier, and F. Renda, "Dynamics of Continuum and Soft Robots: A Strain Parameterization Based Approach," *IEEE Transactions on Robotics,* 2020.

[59] Y. Jiang, D. Chen, C. Liu, and J. Li, "Chain-like granular jamming: a novel stiffness-programmable mechanism for soft robotics," *Soft robotics,* vol. 6, no. 1, pp. 118-132, 2019.

[60] M. Skouras, B. Thomaszewski, B. Bickel, and M. Gross, "Computational design of rubber balloons," in *Computer Graphics Forum*, 2012, vol. 31, no. 2pt4: Wiley Online Library, pp. 835-844.

[61] G. Dämmer, S. Gablenz, A. Hildebrandt, and Z. Major, "Design and shape optimization of PolyJet bellows actuators," in *2018 IEEE International Conference on Soft Robotics (RoboSoft)*, 2018: IEEE, pp. 282-287.

[62] D. M. Bodily, T. F. Allen, and M. D. Killpack, "Multi-objective design optimization of a soft, pneumatic robot," in *2017 IEEE International Conference on Robotics and Automation (ICRA)*, 2017: IEEE, pp. 1864-1871.

[63] G. Runge, J. Peters, and A. Raatz, "Design optimization of soft pneumatic actuators using genetic algorithms," in *2017 IEEE International Conference on Robotics and Biomimetics (ROBIO)*, 2017: IEEE, pp. 393-400.

[64] T. Kurban, P. Civicioglu, R. Kurban, and E. Besdok, "Comparison of evolutionary and swarm based computational techniques for multilevel color image thresholding," *Applied Soft Computing,* vol. 23, pp. 128-143, 2014.

[65] A. H. Gandomi, X.-S. Yang, and A. H. Alavi, "Mixed variable structural optimization using firefly algorithm," *Computers & Structures,* vol. 89, no. 23-24, pp. 2325-2336, 2011.

[66] E. M. de Souza and E. C. N. Silva, "Topology optimization applied to the design of actuators driven by pressure loads," *Structural and Multidisciplinary Optimization,* vol. 61, no. 5, pp. 1763-1786, 2020.

[67] B. Caasenbrood, A. Pogromsky, and H. Nijmeijer, "A Computational Design Framework for Pressure-driven Soft Robots through Nonlinear Topology Optimization," in *2020 3rd IEEE International Conference on Soft Robotics (RoboSoft)*, 2020: IEEE, pp. 633-638.

[68] H. Zhang, A. S. Kumar, J. Y. H. Fuh, and M. Y. Wang, "Design and development of a topology-optimized three-dimensional printed soft gripper," *Soft robotics,* vol. 5, no. 5, pp. 650-661, 2018.

[69] H. K. Hameed, W. Z. Hassan, S. Shafie, S. A. Ahmad, and H. Jaafar, "Soft robotic glove system controlled with amplitude independent muscle activity detection algorithm by using single sEMG channel," in *2018 IEEE 5th International Conference on Smart Instrumentation, Measurement and Application (ICSIMA)*, 2018: IEEE, pp. 1-6.

[70] P. Vela-Anton *et al.*, "Borjibot: A Soft Robotic Device Performing Pressure and Torsional Stimuli for Neonates Oral-Motor Rehabilitation," in *2020 8th IEEE RAS/EMBS International Conference for Biomedical Robotics and Biomechatronics (BioRob)*: IEEE, pp. 403-409.

[71] G. RATENI, "Design and development of a Soft Robotic instrument for manipulation in Minimally Invasive Surgery," 2014.

[72] T. CARELLA, "Design optimization of a passive soft robotic device for neurorehabilitation," 2019.

[73] E. TRIGILI, "Study and development of a soft semi-active rotational joint for wearable robotics," 2015.

[74] Y. Wu, F. Wang, S. Fan, and J. K.-F. Chow, "Robotics in dental implantology," *Oral and Maxillofacial Surgery Clinics,* vol. 31, no. 3, pp. 513-518, 2019.

[75] C. A. Russo, C. Steiner, and W. Spector, "Hospitalizations related to pressure ulcers among adults 18 years and older, 2006: Statistical brief# 64," *Healthcare cost and utilization project (HCUP) statistical briefs,* 2006.

[76] G. Bennett, C. Dealey, and J. Posnett, "The cost of pressure ulcers in the UK," *Age and ageing,* vol. 33, no. 3, pp. 230-235, 2004.

[77] J.-H. Hsiao, J.-Y. Chang, and C.-M. Cheng, "Soft medical robotics: clinical and biomedical applications, challenges, and future directions," *Advanced Robotics,* vol. 33, no. 21, pp. 1099-1111, 2019.

[78] T. Bui, P. Lestriez, D. Pradon, K. Debray, and R. Taiar, "The prevention of pressure ulcers: biomechanical modelization and simulation of human seat cushion contributions," in *International Conference on Advances in Computational Mechanics*, 2017: Springer, pp. 1157-1170.

[79] J. Kottner *et al.*, "Prevention and treatment of pressure ulcers/injuries: The protocol for the second update of the international Clinical Practice Guideline 2019," *Journal of tissue viability,* vol. 28, no. 2, pp. 51-58, 2019.

[80] P. Joyce, Z. E. Moore, and J. Christie, "Organisation of health services for preventing and treating pressure ulcers," *Cochrane Database of Systematic Reviews,* no. 12, 2018.

[81] R. Yousefi *et al.*, "A smart bed platform for monitoring & ulcer prevention," in *2011 4th international conference on biomedical engineering and informatics (BMEI)*, 2011, vol. 3: IEEE, pp. 1362-1366.

[82] G. Fiedler, G. Papaioannou, C. Mitrogiannis, G. Nianios, and T. Kyprianou, "Development of a new bed system with improved decubitus prophylaxis for bed-ridden patients," in *2009 9th International Conference on Information Technology and Applications in Biomedicine*, 2009: IEEE, pp. 1-4.

[83] A. A. Polliack and S. Scheinberg, "A new technology for reducing shear and friction forces on the skin: implications for blister care in the wilderness setting," *Wilderness & environmental medicine,* vol. 17, no. 2, pp. 109-119, 2006.

[84] A. Cheung and E. Tam, "Relationship between body weight and tissue thickness over the ischial tuberosities and the sacrum," 2003.

[85] F. Romano and G. Zingone, "Deflections of beams with varying rectangular cross section," *Journal of engineering mechanics,* vol. 118, no. 10, pp. 2128-2134, 1992.

[86] O. Bauchau and J. Craig, "Euler-Bernoulli beam theory," in *Structural analysis*: Springer, 2009, pp. 173-221.

[87] H. Lipson, "Challenges and opportunities for design, simulation, and fabrication of soft robots," *Soft Robotics,* vol. 1, no. 1, pp. 21-27, 2014.

[88] H. K. Yap, H. Y. Ng, and C.-H. Yeow, "High-force soft printable pneumatics for soft robotic applications," *Soft Robotics,* vol. 3, no. 3, pp. 144-158, 2016.

[89] "EZ-SIL RTV Silicone Rubber, Translucent,Shore A 25,Mold Making (Trial Size(2.2 lbs))." [Online]. Available: https://www.amazon.com/EZ-SIL-Silicone-Rubber-Translucent-Making/dp/B081NVD9BT/ref=sr_1_1?keywords=silicone+shore+A+25&qid=1577738376&s=arts-crafts&sr=1-1.

[90] "ZHERMACK Elite Double 22." [Online]. Available: https://chasedentalsupply.com/elite-double-22-standard-pack.aspx?_vsrefdom=adwords&gclid=CjwKCAjwiOv7BRBREiwAXHbv3Kmg6AHP9oVUCWR-B8ImLsOu0n5z1qA7LX1WuH04k0FTh1aODhTkOhoChg0QAvD_BwE.

[91] K. Hibbert, G. Warner, C. Brown, O. Ajide, G. Owolabi, and A. Azimi, "The effects of build parameters and strain rate on the mechanical properties of FDM 3D-Printed acrylonitrile Butadiene Styrene," *Open Journal of Organic Polymer Materials,* vol. 9, no. 01, p. 1, 2019.

[92] M. Shahzad, A. Kamran, M. Z. Siddiqui, and M. Farhan, "Mechanical characterization and FE modelling of a hyperelastic material," *Materials Research,* vol. 18, no. 5, pp. 918-924, 2015.

[93] E. Shahriari, W. M. M. Yunus, K. Naghavi, and E. Saion, "The optical nonlinearity of Au and Ag nanoparticle prepared by the γ-radiation method," *Am. J. Eng. Appl. Sci,* vol. 3, no. 2, pp. 232-236, 2010.

[94] A. N. Gent, *Engineering with rubber: how to design rubber components*. Carl Hanser Verlag GmbH Co KG, 2012.

[95] R. Rivlin, "Large elastic deformations of isotropic materials. I. Fundamental concepts," *Philosophical Transactions of the Royal Society of London. Series A, Mathematical and Physical Sciences,* vol. 240, no. 822, pp. 459-490, 1948.

[96] F. Peeters and M. Kussner, "Material law selection in the finite element simulation of rubber-like materials and its practical application in the industrial design process," *Constitutive models for rubber,* vol. 1, pp. 29-36, 1999.

[97] O. H. Yeoh, "Some forms of the strain energy function for rubber," *Rubber Chemistry and technology,* vol. 66, no. 5, pp. 754-771, 1993.

[98] L. Guo and Y. Wang, "High-rate tensile behavior of silicone rubber at various temperatures," *Rubber Chemistry and Technology,* vol. 93, no. 1, pp. 183-194, 2020.

[99] T. R. Chandrupatla and A. D. Belegundu, "Introduction to Finite Elements in Engineering, PHI Learning Pvt," *Limited, New Delhi,* 2011.

[100] J. Bard, "A Review of:“Engineering Optimization: Theory and Practice, ” Singiresu S. Rao John Wiley & Sons, Inc., 1996, 903 pp., $95.00, ISBN 0471550345," *Iie Transactions,* vol. 29, no. 9, pp. 802-803, 1997.

[101] H. W. Berhe, "Penalty function methods using matrix laboratory (MATLAB)," *African Journal of Mathematics and Computer Science Research,* vol. 5, no. 13, pp. 209-246, 2012.

[102] O. Kramer, "Iterated local search with Powell's method: a memetic algorithm for continuous global optimization," *Memetic Computing,* vol. 2, no. 1, pp. 69-83, 2010.

[103] X.-S. Yang, "Firefly algorithm, stochastic test functions and design optimisation," *International journal of bio-inspired computation,* vol. 2, no. 2, pp. 78-84, 2010.

[104] M. Kazemzadeh-Parsi, "A modified firefly algorithm for engineering design optimization problems," *Iranian Journal of Science and Technology. Transactions of Mechanical Engineering,* vol. 38, no. M2, p. 403, 2014.

[105] X.-S. Yang, "FireFly Algorithm," 2021. [Online]. Available: https://www.mathworks.com/matlabcentral/fileexchange/29693-firefly-algorithm.

[106] C. Choi, W. Schwarting, J. DelPreto, and D. Rus, "Learning object grasping for soft robot hands," *IEEE Robotics and Automation Letters,* vol. 3, no. 3, pp. 2370-2377, 2018.

[107] T. Yang *et al.*, "A soft artificial muscle driven robot with reinforcement learning," *Scientific reports,* vol. 8, no. 1, pp. 1-8, 2018.

[108] S. Bhagat, H. Banerjee, Z. T. Ho Tse, and H. Ren, "Deep reinforcement learning for soft, flexible robots: brief review with impending challenges," *Robotics,* vol. 8, no. 1, p. 4, 2019.

[109] X. Y. Lee, A. Balu, D. Stoecklein, B. Ganapathysubramanian, and S. Sarkar, "A case study of deep reinforcement learning for engineering design: Application to microfluidic devices for flow sculpting," *Journal of Mechanical Design,* vol. 141, no. 11, 2019.

[110] K. Yonekura and H. Hattori, "Framework for design optimization using deep reinforcement learning," *Structural and Multidisciplinary Optimization,* vol. 60, no. 4, pp. 1709-1713, 2019.

[111] J. Viquerat, J. Rabault, A. Kuhnle, H. Ghraieb, A. Larcher, and E. Hachem, "Direct shape optimization through deep reinforcement learning," *Journal of Computational Physics,* vol. 428, p. 110080, 2021.

[112] M. Sewak, *Deep reinforcement learning*. Springer, 2019.

[113] T. P. Lillicrap *et al.*, "Continuous control with deep reinforcement learning," *arXiv preprint arXiv:1509.02971,* 2015.

[114] A. Hill *et al.*, "Stable baselines," ed, 2018.

[115] A. Kaszynski, "pyansys: Python Interface to MAPDL and Associated Binary and ASCII Files," *Zenodo,* 2020. [Online]. Available: https://zenodo.org/record/4009467.

[116] S. E. Benzley, E. Perry, K. Merkley, B. Clark, and G. Sjaardama, "A comparison of all hexagonal and all tetrahedral finite element meshes for elastic and elasto-plastic analysis," in *Proceedings, 4th international meshing roundtable*, 1995, vol. 17: Citeseer, pp. 179-191.

[117] J. Brauer, *What every engineer should know about finite element analysis*. CRC Press, 1993.

[118] F. Mathieu, F. Hild, and S. Roux, "Identification of a crack propagation law by digital image correlation," *International Journal of Fatigue,* vol. 36, no. 1, pp. 146-154, 2012.

[119] N. McCormick and J. Lord, "Digital image correlation," *Materials today,* vol. 13, no. 12, pp. 52-54, 2010.

[120] G. Crammond, S. Boyd, and J. Dulieu-Barton, "Speckle pattern quality assessment for digital image correlation," *Optics and Lasers in Engineering,* vol. 51, no. 12, pp. 1368-1378, 2013.

[121] M. Grujicic, B. Pandurangan, G. Arakere, W. Bell, T. He, and X. Xie, "Seat-cushion and soft-tissue material modeling and a finite element investigation of the seating comfort for passenger-vehicle occupants," *Materials & Design,* vol. 30, no. 10, pp. 4273-4285, 2009.

[122] Aquilacorp.com, "Airpulse PK2 Custom Wheelchair Cushion," 2021. [Online]. Available: https://aquilacorp.com/products/airpulse-pk2/.

[123] R. Rajamani, "SENSORS AND SENSING SYSTEMS," *NSF,* 2009. [Online]. Available: https://www.nsf.gov/awardsearch/showAward?AWD_ID=0856387.

[124] M. Arashi *et al.*, "Vibration therapy accelerates healing of Stage I pressure ulcers in older adult patients," *Advances in skin & wound care,* vol. 23, no. 7, pp. 321-327, 2010.

[125] S. Ostadabbas. [Online]. Available: https://www.nsf.gov/awardsearch/showAward?AWD_ID=1755695.